

**Development of a 10-year (2001–2010) 0.1-degree dataset of land-surface energy balance
for mainland China**

Xuelong Chen^a, Zhongbo Su^a, Yaoming Ma^b, Shaomin Liu^c, Qiang Yu^d, Ziwei Xu^c

^a Faculty of Geo-Information Science and Earth Observation, University of Twente, Enschede,
The Netherlands

^b Key Laboratory of Tibetan Environment Changes and Land Surface Processes, Institute of
Tibetan Plateau Research, Chinese Academy of Sciences, Beijing, China

^c State Key Laboratory of Remote Sensing Science, School of Geography, Beijing Normal
University, Beijing, China

^d Plant Functional Biology & Climate Change Cluster, University of Technology, Sydney, PO
Box 123, Broadway, NSW 2007, Australia

Abstract

In the absence of high resolution estimates of the components of surface energy balance for China, we developed an algorithm based on the surface energy balance system (SEBS) to generate a dataset of land-surface energy and water fluxes on a monthly time scale from 2001 to 2010 at a 0.1×0.1 degree spatial resolution by using multi-satellite and meteorological forcing data. A remote-sensing-based method was developed to estimate canopy height, which was used to calculate roughness length and flux dynamics. The land-surface flux dataset was validated against “ground-truth” observations from 11 flux tower stations in China. The estimated fluxes correlate well with the stations’ measurements for different vegetation types and climatic

conditions (average bias = 15.3 Wm^{-2} , RMSE = 26.4 Wm^{-2}). The quality of the data product was also assessed against the GLDAS dataset. The results show that our method is efficient for producing a high-resolution dataset of surface energy flux for the Chinese landmass from satellite data. The validation results demonstrate that more accurate downward long-wave radiation datasets are needed to be able to accurately estimate turbulent fluxes and evapotranspiration when using the surface energy balance model. Trend analysis of land-surface radiation and energy exchange fluxes revealed that the Tibetan Plateau has undergone relatively stronger climatic change than other parts of China during the last 10 years. The capability of the dataset to provide spatial and temporal information on water-cycle and land-atmosphere interactions for the Chinese landmass is examined. The product is free to download for studies of the water cycle and environmental change in China.

35

36 1. Introduction

As China is one of the fastest growing and urbanizing economies in the world, changes in land cover and land use can significantly influence the environment by altering land-atmosphere energy and water exchanges (Suh and Lee, 2004; Lin et al., 2009). For instance, rapid urban expansion has substantially changed [land](#) surface heat fluxes in the Pearl River delta (PRD) (Lin et al., 2009) and has increased sensible heat fluxes in the Beijing metropolitan area (Zhang et al., 2009a). The variability of surface energy balance and its partitioning may also have an important impact on climate variability in China (Sun and Wu, 2001). Similarly, changes in surface energy fluxes have been shown to alter the intensity of the East Asian monsoon (Zhou and Huang, 2008; Qiu, 2013; Hsu and Liu, 2003). In short, understanding variation in energy fluxes is

46 important for the study of climate change in China (Brauman et al., 2007). Nevertheless, the
47 spatial and temporal variability of China's land-surface energy balance, and the magnitude of
48 each, are still unknown.

49 While it is of critical importance to understand the partitioning of water and energy distribution
50 across China's terrestrial surface, accurate monitoring of their spatial and temporal variation is
51 notoriously difficult (Ma et al., 2011). Several field experiments are being carried out to monitor
52 turbulent fluxes over selected land cover in China by using ground-based eddy covariance
53 devices (Wang et al., 2010; Yu et al., 2006; Ma et al., 2008b; Li et al., 2009). However, these
54 measurements are only representative of small areas around the locations where the
55 measurements are being made. For this reason, establishment of an eddy-covariance flux
56 network cannot provide a complete land-surface heat flux picture for the entire Chinese landmass.

57 A number of ~~methods can be used to products can be derived from~~ land-surface energy fluxes.
58 Jung et al. (2009), for example, generated global spatial flux fields by using a network up-scaling
59 method. However their flux network included only a limited number of flux stations in China.
60 The Global Soil Wetness Project 2 (GSWP-2) (Dirmeyer et al., 2006) produced a global land
61 surface product on a 1×1 degree grid for the period 1986 to 1995. The Global Land Data
62 Assimilation System (GLDAS) (Rodell et al., 2004) can provide a global coverage in the form of
63 3-hourly, 0.25-degree data. Furthermore, products from the European Centre for Medium-Range
64 Weather Forecasts (ECMWF) interim reanalysis (ERA-Interim) (Dee et al., 2011), the National
65 Centers for Environmental Prediction (NCEP) (Kalnay et al., 1996), Modern-Era Retrospective
66 Analysis for Research and Applications (MERRA) (Rienecker et al., 2011) and other reanalysis
67 data can also provide temporally continuous – but coarse – spatial resolution datasets of land

68 surface fluxes. Jiménez et al. (2011) made an inter-comparison of different land-surface heat flux
69 products. When these products were applied at continental scales, the different approaches
70 resulted in large differences (Vinukollu et al., 2011a; Jiménez et al., 2011; Mueller et al., 2011).

71 The problems met by using currently available flux data in climate studies of China have been
72 reported by Zhou and Huang (2010). Zhu et al. (2012) have also reported that summer sensible
73 heat flux derived from eight datasets (including NCEP, ERA, and GLDAS) of China's Tibetan
74 Plateau region differ from each other in their spatial distribution. In addition, all the flux datasets
75 mentioned above are based on model simulations, which have deficiencies for studying changes
76 in water-cycle and land-air interactions in China (Chen et al., 2013c; Su et al., 2013; Wang and
77 Zeng, 2012; Ma et al., 2008a).

78 A spatially and temporally explicit estimate of surface energy fluxes is of considerable interest
79 for hydrological assessments and meteorological and climatological investigations (Norman et
80 al., 2003). Satellite-sensed data of surface variables can be used to produce maps of heat and
81 water fluxes at different scales (Wang and Liang, 2008; Li et al., 2012a; Liu et al., 2010; Vinukollu
82 et al., 2011b). Remote sensing approaches to estimate surface heat and water fluxes have been
83 largely used on regional scales (Fan et al., 2007; Ma et al., 2011; Jia et al., 2012; Zhang et al.,
84 2009b; Li et al., 2012b; Shu et al., 2011), but there is no analysis of satellite-derived data currently
85 underway to produce a complete, physically-consistent, decadal land-surface heat flux dataset
86 (Jiménez et al., 2009) for the Chinese landmass. The use of remotely-sensed data offers the
87 potential of acquiring observations of variables such as albedo, land surface temperature, and
88 NDVI at a continental scale for China. ~~Figure 1 shows an example of an NDVI map for China.~~

89

90 Since surface fluxes cannot be directly detected by satellite-borne sensors, an alternative for
91 estimating continental water and energy fluxes can be derived by applying the aerodynamic
92 theory of turbulent flux transfer (Ma et al., 2011) or by establishing statistical relationships
93 between related satellite observations and land surface fluxes (Jiménez et al., 2009; Wang et al.,
94 2007). Most remotely-sensed latent heat flux or evapotranspiration products have null values in
95 urban, water, snow, barren and desert areas (Mu et al., 2007; Wang et al., 2007; Jiménez et al.,
96 2009). This is due to the lack of a uniform representation of turbulent exchange processes over
97 different types of land cover in their method. Meanwhile, the aerodynamic turbulent transfer
98 method can describe the flux exchange through changes in surface roughness length over
99 different land covers. Statistical methods establish relationships between satellite-sensed
100 observations (e.g. *NDVI*, *LST*, albedo) and land surface fluxes through various fitting techniques
101 (Wang et al., 2007). The simple relationships established cannot give a reasonable approximation
102 for extreme conditions such as bare soil or other types of non-canopy land cover (e.g. lakes,
103 deserts) because land covers behave significantly differently in land-surface energy flux
104 partitioning. Fortunately, turbulent flux transfer parameterization can overcome the shortcomings
105 of statistical methods and produce spatially continuous distributions of land-surface energy
106 fluxes with prepared meteorological forcing data. For this reason we chose a more physically-
107 based method – turbulent flux parameterization – to produce the dataset.

108 The challenge in using turbulent flux parameterization lies in the transition from regional to
109 continental and global scales, because meteorological data of high resolution (i.e. 1–10 km) are
110 not easily obtained for a large region. Recently, Chinese scientists have produced high resolution
111 meteorological forcing data that can be used in our study. Another issue is the complexity met
112 with the method when combining different spatial and temporal sampling input variables. This is

discussed in detail in Subsection 3.1. The last difficulty that has surrounded application of turbulent flux parameterization at continental scales is the acquisition of roughness length. To address this difficulty, we have developed a remote-sensing-based mixing technique to estimate canopy heights at a continental scale and use the resulting canopy height dataset to derive, for the very first time, the dynamic variation of surface roughness length for the Chinese landmass.

Complex topography (shown by Fig. 1) and climatic conditions in China make it very difficult to obtain a clear picture of the distribution of energy and water fluxes with a high spatial resolution over a relatively long period for such a large area. In our study we ~~set out to~~ estimate

~~turbulent~~land-surface heat fluxes simulated with energy balance and aerodynamic parameterization formulas that are based on a revised model of the surface energy balance system (SEBS) (Chen et al., 2013b;Chen et al., 2013a;Su, 2002;Timmermans, 2011); Previous tests show that the revised model delivers better performance and improvements in cases where the type of land cover in China is bare soil, short canopy or snow (Chen et al., 2013b;Chen et al., 2013a). Sensible heat flux in SEBS was derived from the difference between surface temperature and air temperature by using Monin–Obukhov similarity theory and bulk atmospheric boundary layer similarity (Brutsaert, 1999), which parameterizes ground surface momentum and heat-transfer coefficient maps to take into account surface roughness, canopy height, vegetation cover, and meteorological stability (Su et al., 2001;Su, 2002;Chen et al., 2013b). The latent heat flux can then be estimated from an energy balance model, assuming surface net radiation and ground flux are known (Ma et al., 2002;Allen et al., 2011;Vinukollu et al., 2011b). We used high resolution reanalysis data, which merges model outputs, remote sensing observations, and in-situ measurements. In addition, we also assessed the accuracy of the surface energy balance terms

135 (net radiation, sensible heat, latent heat, and ground heat fluxes) and their climatic trends in the
136 preceding decade (2001–2010).

137 After defining the equations of the SEBS model (Section 2), we describe (in Section 3) the input
138 data and ground-truth measurements used in the study. Further, we assess the capacity of the
139 remote-sensing-based product to reproduce the range and variability of measured fluxes by
140 comparing them with in-situ flux tower measurements, followed by trend analysis of the spatial
141 patterns of the fluxes (Section 4). Concluding remarks are found in Section 5.

142

143 **2 Model description and development**

144 The surface energy balance system model known as SEBS (Su, 2002) uses aerodynamic
145 resistance to create a spatially coherent estimate of land surface heat fluxes. Some model inputs
146 can be obtained from remote sensing data, while others can be obtained from meteorological
147 forcing data (e.g. GLDAS, ERA and NCEP reanalysis data). The model's equations and the
148 required forcing variables are described in the remainder of this section.

149 The surface energy balance equation can be expressed as:

$$150 \quad Rn = G_0 + H + LE, \quad (1)$$

151 where Rn is the net radiation flux; G_0 is the ground heat flux, which is parameterized by its
152 relationship with Rn (Su et al., 2001); H is the sensible heat flux; and LE is the latent heat flux.

153 LE is computed by using the evaporative fraction after deriving the other three variables in
154 Equation 1 and taking into consideration energy and water limits (Su, 2002). As these fluxes were

155 produced with a monthly average temporal resolution, energy storage in vegetation is not
156 considered.

157

158 Net radiation flux is:

$$159 \quad Rn = (1 - \alpha) \times SWD + LWD - LWU, \quad (2)$$

160 where α is broadband albedo; SWD is downward surface short-wave radiation; and LWD and LWU
161 are downward and upward surface long-wave radiation, respectively.

162 Here satellite observed albedo is used. LWU is derived from land surface temperature (LST) using
163 the Stefan–Boltzmann law. Land surface emissivity is derived as described in Chen et al. (2013a).
164 LWD and SWD values are obtained from meteorological forcing data.

165

166 Sensible heat flux (H) is computed according to the Monin–Obukhov similarity theory (MOST):

$$167 \quad H = k u_* \rho C_p (\theta_0 - \theta_a) \left[\ln \left(\frac{z-d}{z_{0h}} \right) - \Psi_h \left(\frac{z-d}{L} \right) + \Psi_h \left(\frac{z_{0h}}{L} \right) \right]^{-1}, \quad (3)$$

168 where k is the von Karman constant; u_* is friction velocity; ρ is air density; C_p is specific heat for
169 moist air; θ_0 is the potential temperature at the ground surface; θ_a is the potential air temperature
170 at height z ; d is the zero plane displacement height; Ψ_h is the stability correction function for
171 sensible heat transfer (Brutsaert, 1999); and L is the Obukhov length. In our study θ_a was obtained
172 from meteorological forcing data and θ_0 was derived from Moderate Resolution Imaging
173 Spectroradiometer (MODIS) LST data. For more detailed information about u_* and the calculation
174 of L , see Su (2002) and Chen et al. (2013b).

175

176 The roughness height for heat transfer (z_{0h}) in Equation 3 is calculated as follows:

$$z_{0h} = \frac{z_{0m}}{\exp(kB^{-1})}. \quad (4)$$

Using the fractional canopy coverage, kB^{-1} at each pixel can be derived according to the following modification of the equation described by Su et al. (2001):

$$kB^{-1} = f_c^2 \times kB_c^{-1} + f_s^2 \times kB_s^{-1} + 2 \times f_c \times f_s \times kB_m^{-1}, \quad (5)$$

where f_c is fractional canopy coverage and f_s is the fraction of bare soil in one pixel; kB_c^{-1} is the kB^{-1} of the canopy; kB_s^{-1} is the kB^{-1} of bare soil; and kB_m^{-1} is kB^{-1} for mixed bare soil and canopy. As kB^{-1} is the most important parameter in a MOST-based calculation of sensible heat flux, kB^{-1} has been updated by Chen et al. (2013b). The momentum roughness length used to calculate kB_s^{-1} was given a value of 0.004 (Chen et al., 2013b), and the heat roughness length of bare soil was calculated according to Yang et al. (2002). The new kB^{-1} gives a better performance than the previous version of kB^{-1} (Chen et al., 2013b; Chen et al., 2013a). Detailed evaluations of the new parameterization of kB^{-1} can be found in Chen et al. (2013b).

The roughness height for momentum transfer z_{0m} in Equation 4 is derived from canopy height (HC), leaf area index (LAI) and the canopy momentum transfer model (Massman, 1997):

$$z_{0m} = HC \times (1 - d/HC) \times \exp(-k \times \beta), \quad (6)$$

$$\beta = C_1 - C_2 \times \exp(-C_3 \times C_d \times LAI), \quad (7)$$

where $C_1 = 0.32$, $C_2 = 0.26$, and $C_3 = 15.1$ are model constants related to the bulk surface drag coefficient (Massman 1997). The three constants have been tested for several canopies (Chen et al., 2013b; Cammalleri et al., 2010) and evaluated as one of the best solutions for canopy turbulent-flux parameterization (Cammalleri et al., 2010). C_d is the drag coefficient, which typically equals 0.2 (Goudriaan, 1977); d is displacement height, which is derived from HC and the wind speed extinction coefficient (Su, 2002; Su et al., 2001).

199

200 As Chen et al. (2013b) have pointed out, HC is vital for turbulent heat simulations, which makes
201 accurate estimation of HC for the Chinese landmass important for this study. A remote-sensing-
202 based canopy height method (Chen et al., 2013b) was further developed to estimate canopy height
203 distribution for the whole China [in this study](#). Simard et al. (2011) produced a global forest
204 canopy-height map using data from the Geoscience Laser Altimeter System (GLAS) aboard
205 ICESat (Ice, Cloud, and land Elevation Satellite). However, short-canopy (e.g. maize, rice, wheat)
206 height information cannot be acquired by laser techniques. Since short-canopy height usually
207 varies by season throughout the year – crops are planted in spring and harvested in autumn – we
208 calculated short-canopy height using an NDVI-based equation from Chen et al. (2013b):

$$HC = HC_{min} + \frac{HC_{max} - HC_{min}}{(NDVI_{max}(x,y) - NDVI_{min}(x,y))} \times (NDVI(x,y) - NDVI_{min}(x,y)) ,$$

(8)

211 where HC_{max} and HC_{min} are the maximum and minimum short-canopy height; HC_{min} is set to
212 0.002 m; and HC_{max} is set to 2.5 m, corresponding to the greatest height of seasonal crops in
213 China. $NDVI_{min}$ and $NDVI_{max}$ are [a matrix of](#) minimum and maximum NDVI values during our
214 10-year study period. Each short-canopy pixel was given an $NDVI_{min}$ and $NDVI_{max}$ value to
215 calculate the canopy height. The NDVI-based short-canopy height method above was used to fill
216 relevant pixels with forest canopy heights of less than 10 m. Higher canopy heights (greater than
217 10 m) were assumed to be constant, i.e. with no seasonal change. By merging canopy heights
218 greater than 10 m and variable short-canopy data, we constructed dynamic monthly maps of
219 canopy heights for the Chinese landmass for the period of 2001–2010. These maps were then

Formatted: Automatically adjust right indent when grid is defined, Space After: 10 pt, Adjust space between Latin and Asian text, Adjust space between Asian text and numbers

used to calculate [land surface](#) heat fluxes. [Figure 2 gives an example of derived canopy height at 11 China flux stations.](#)

3 Data and validation

Our modeling approach makes use of a variety of satellite-based sensor data and meteorological forcing data to estimate monthly energy and water fluxes across China. The forcing data can come from satellite-based or reanalysis datasets. Due to the influence of weather, satellite-sensed visible and thermal band data (e.g. NDVI, albedo, LST) often have spatial and temporal gaps in daily data. Various temporal and spatial gap-filling algorithms have been developed to produce continuous monthly data for satellite-sensed variables (Chen et al., 2004; Moody et al., 2005). In order to avoid both spatial and temporal gaps in the final product, we selected some specific satellite-sensed datasets for this study (see Table 1). Detailed information about each input variable is described in following subsections.

The longest period covered by the forcing dataset is approximately 31 years; the shortest is about 10 years. Spatial resolution of the dataset varies from 0.01 to 0.25 degrees and its sample frequency from 3 hours to 1 month. The meteorological forcing data developed by the Institute of Tibetan Plateau Research, Chinese Academy of Sciences (hereafter referred to as ITPCAS forcing data) (He, 2010) was constructed to study meteorological variation in China. ITPCAS forcing data covers the entire landmass of China and has the highest temporal resolution among the input datasets used. Other variables such as LST and albedo, for example, have coarser temporal resolutions (monthly) and global coverage. When combining data of different spatial and temporal resolutions, both spatial and temporal scaling issues need to be addressed.

243

244 Estimates of land-surface energy flux can be subject to large errors, due to bias in the
245 meteorological forcing input data. The spatial distribution of meteorological variables is closely
246 related to topography (Li et al., 2013). When interpolating meteorological input variables to finer
247 scales, these effects have to be accounted for (Sheffield et al., 2006), which goes beyond the
248 scope of our study. Therefore we chose to resample the satellite product of high spatial resolution
249 to a lower spatial resolution that matches the resolution of the meteorological input data. Also,
250 the meteorological data were averaged to monthly values that have the same temporal resolution
251 as the remotely-sensed input variables. ITPCAS forcing data provides us data of the highest
252 spatial resolution among the meteorological forcing data currently available (e.g. ERA-interim,
253 NCEP, GLDAS, MERRA). Taking into account of all these items, our aim was to produce a
254 monthly product of 0.1×0.1 degree resolution land-surface heat fluxes that contains neither
255 spatial nor temporal gaps and can be used to study seasonal and inter-annual variability in the
256 hydrological and energy cycles of China.

257

258 | **3.1 Input datasets and its validations**

259 **3.1.1 Meteorological forcing data**

260 In studies previous to ours, reanalysis data have been applied in many different ways, for example
261 to construct land-surface forcing data (Sheffield et al., 2006), to detect climate trends (Taniguchi
262 and Koike, 2008), and to investigate water and energy cycles at regional and continental scales
263 (Roads and Betts, 2000). Reanalysis data has also been applied by the remote sensing community
264 to derive estimates of global terrestrial evapotranspiration and gross primary production (Mu et al.,
265 2007; Yuan et al., 2010). Few studies, however, have used reanalysis data together with remotely-

266 sensed ground data to derive global land-energy fluxes (sensible heat flux, latent heat flux, net
267 radiation, etc.).

268

269 Researchers have developed several kinds of reanalysis data. Comparisons and evaluations of
270 these reanalysis products with in-situ observations have been performed for individual sites,
271 specific regions, and the entire globe (Wang and Zeng, 2012; Decker et al., 2011). It is well known
272 that inaccuracies existing in reanalysis forcing data may have substantial impacts on the
273 simulation of land-surface energy partitioning. It is difficult to choose which reanalysis data is
274 better for use as forcing data. Additionally, the spatial resolution of all of the above
275 reanalysis/forcing datasets is not as high as that of remote sensing data. The ITPCAS forcing
276 dataset was produced by merging a variety of data sources. This dataset benefits in particular from
277 the merging of information from 740 weather stations operated by the China Meteorological
278 Administration that have not been used in other forcing data. The dataset has already been used to
279 run land surface models and has been shown to be more accurate than other forcing datasets (Chen
280 et al., 2011; Liu and Xie, 2013). ITPCAS meteorological forcing data include variables such as
281 instantaneous near-surface air temperature (T_a), near-surface air pressure (P), near-surface air
282 specific humidity (Q), near-surface wind speed (W_s) at a temporal resolution of 3 hours, 3-hourly
283 mean downward surface short-wave (SWD) and downward surface long-wave (LWD) radiation.
284 The time period covered is from 1979 to 2010; the spatial resolution has a grid size of 0.1×0.1
285 degrees.

286

287 | **3.1.2 MODIS ~~IS11C3~~ land surface temperature processing**

288 MODIS (Moderate-resolution Imaging spectroradiometer) sensors have been used to produce
289 several global and continental scale LST datasets. MOD11C3 V5 ~~and MYD11C3 V5~~ products
290 (Wan, 2009) are validated over a range of representative conditions with an average bias of less
291 than 1 Kelvin (Coll et al., 2009; Wan and Li, 2008). The MOD11C3 V5 ~~monthly~~ LST product,
292 ~~MOD11C3 and MYD11C3~~, has a 0.05-degree grid size, ~~a monthly temporal resolution~~ without
293 gaps and covers the period March 2000 to ~~October 2012~~ near present. It provides monthly daytime
294 and night-time LST values. In our study we averaged the daytime and night-time values of
295 MOD11C3 and MYD11C3 to represent monthly means.

296
297 After spatially interpolating the monthly ~~MOD11C3 V5~~ mean LST from 0.05 × 0.05 degree to a 0.1
298 × 0.1 degree resolution, we picked out LST values of pixels that included the 11 flux tower
299 stations from which in-situ measurements were gathered. The time series comparisons of LST
300 with the ground measurements were shown by Fig. 2. It shows that the processed monthly LST
301 can presented the seasonal variations in LST over different land covers very well. The pixel values
302 were validated against the in-situ LST measurements. Detailed information about each station is
303 given in Subsection 3.2. The linear correlation ($R = 1.0$), RMSE ($= 1.9\text{ K}$) and MB (mean value of
304 the satellite data minus in-situ observation $= 0.5\text{ K}$) indicate that the quality of the merged
305 remotely-sensed monthly LST data in China is high. They also show that MOD11C3 V5 LST
306 captures the in-situ LST variability of different elevations and land surfaces, which is described in
307 Subsection 4.1.

308

309 3.1.3 Albedo

310

Formatted: Font color: Auto

Formatted: Font: 12 pt

Field Code Changed

Field Code Changed

Formatted: Font color: Auto

Formatted: Font color: Auto

Land surface albedo determines the fraction of short-wave radiation absorbed by the ground, thus influencing the surface energy budget. Studies of land-surface energy balance require temporal and spatial albedo input data without gaps. Several research projects have been devoted to producing long-term time series of surface albedo from various satellite-borne sensors (Riihel et al., 2013; Muller et al., 2012; Liu et al., 2013a). However most of the albedo products do not provide gap-filled time-series albedo maps. Taking MODIS MCD43B albedo product as an example, 20 to 40% of the pixels of global landmass miss valid albedo values every year (Liu et al., 2013a). Twenty percent invalid values in albedo input data will result in the same amount of empty values in ~~heat flux~~ output, an issue that limits albedo data that can be used in our study. After checking several albedo products (including GlobAlbedo (Muller et al., 2012), CMSAF cClouds, Albedo and RAdiation Surface Albedo (CLARA-SAL albedo) (Riihel et al., 2013), and MCD43B), we decided to use GlobAlbedo as its data does not contain spatial or temporal gaps. This albedo dataset is based on a monthly sample and has a spatial resolution of 0.05 degrees, which we interpolated to a 0.1 degree resolution for our study.

3.1.4 NDVI

The Normalized Difference Vegetation Index (NDVI) is regarded as a reliable indicator of vegetation parameters. NDVI has been widely used to explore vegetation dynamics and their relationships with environmental factors (Piao et al., 2006). NDVI data from the Systeme Pour l’Observation de la Terre (SPOT) VEGETATION sensor, distributed by Vito, have a spatial resolution of 1 km × 1 km and a temporal resolution of 10 days (synthesized on days 1, 11 and 21 of each month). In order to reduce noise resulting from clouds, the maximum NDVI value in a month for each pixel is selected to represent the canopy status of that month.

334

335 | **3.1.5 Canopy fraction**

Formatted: Font color: Red

336 Canopy fraction (f_c) is defined as the fraction of ground surface covered by the vegetation
337 canopy (varying from 0 to 1). f_c in SEBS is used to distinguish the contributions of vegetation
338 and soil to the roughness parameterization. Here f_c was derived from NDVI data using the
339 following equation:

$$f_c = \frac{NDVI - NDVI_{min}}{NDVI_{max} - NDVI_{min}} .$$

340 **3.2 Validation data**

341 The product generated by our model needed to be validated by comparing it with an independent
342 observational dataset. The energy balance measurement system (eddy covariance, four
343 component radiation and ground heat flux) at flux sites is widely accepted as a method for direct
344 measurement of energy and fluxes and is widely applied for assessing global evapotranspiration
345 products (Zhang et al., 2010;Jung et al., 2011;Yan et al., 2012;Fisher et al., 2008).

346 To validate the product, we compiled a dataset from 11 flux stations in China with land cover
347 types including bare soil, alpine meadow, forest, cropland, orchard, grassland, and wetlands.
348 Elevations of these stations range from 5 m to 4800 m. The observational dataset includes data
349 from Maqu (MQ) (Chen et al., 2013b;Wang et al., 2013), Wenjiang (WJ) (Zhang et al., 2012),
350 Bijie (BJ) (Ma et al., 2006), Miyun (MY) (Liu et al., 2013b), Daxing (DX) (Liu et al., 2013b),
351 Guantao (GT) (Liu et al., 2011;Liu et al., 2013b), Yucheng (YC) (Flerchinger et al., 2009),
352 Dongtan (DT) (Zhao et al., 2009), SC (Semi-Arid Climate and Environment Observatory of
353 Lanzhou University) (Huang et al., 2008;Wang et al., 2010;Guan et al., 2009), and Weishan (WS)
354 stations (Lei and Yang, 2010b, a). Detailed information about each site is listed in Table 2.

355 Half-hourly fluxes were processed using standardized quality control procedures, which are
356 described in the literature references for each station. The half-hourly H, LE, and four
357 component radiation were then averaged to monthly values. Monthly average values derived
358 from less than 70% of the flux data in each month were not used in the validations. Gap filling
359 was not used for the flux measurement data.

360 4 Results

361 4.1 Canopy height assessment

362 We checked the canopy height variations at the 10 flux station produced by equation 8 and GLAS
363 forest height (Figure 3). The derived canopy height for AL is not higher than 0.2 m, which is
364 reasonable for the local land cover. YC, GT, and WS station located in the North China,
365 represent a typical agricultural land, where has crops mature twice per year. The highest canopy
366 height is around 1.5 m, the same height as maize in summer. The fall-down step in June at these
367 three stations is due to wheat/maize is harvested and new seeds is sown during this period. This
368 step variation in the canopy height also cause similar step changes in sensible and latent heat flux
369 (shown by Fig. 5). Although the land cover near WJ station is crops. It is more surround by
370 forest in a 10 km diameter. The GLAS forest height reflects this ground truth. These canopy
371 height assessment at the observation sites makes us take the developed method in this work as an
372 appropriate one for solving scarcity of canopy height information at a continental area.

373 4.2 Validation against flux tower measurements

Formatted: Font: Times New Roman, 12 pt, Bold

Formatted ... [1]

Formatted: Font: Times New Roman, 12 pt

Formatted: Font: Times New Roman, 12 pt

Formatted: Font: Times New Roman, 12 pt

Formatted: Font: Times New Roman, 12 pt

Formatted: Font: Times New Roman, 12 pt

Formatted: Font: Times New Roman, 12 pt

Formatted: Font: Times New Roman, 12 pt

Formatted: Font: Times New Roman, 12 pt

Formatted: Font: Times New Roman, 12 pt

Formatted: Font: Times New Roman, 12 pt

Formatted: Font: Times New Roman, 12 pt

Formatted: Font: Times New Roman, 12 pt

Formatted: Font: Times New Roman, 12 pt

Formatted: Font: Times New Roman, 12 pt

Formatted: Font: Times New Roman, 12 pt

Formatted: Font: Times New Roman, 12 pt

Formatted: Font: Times New Roman, 12 pt

Formatted: Font: Times New Roman, 12 pt

Formatted: Font: Times New Roman, 12 pt, Bold

374 The accuracy of remote-sensing-based land-surface heat fluxes is questionable without validation
375 against ground-based measurements (Meir and Woodward, 2010). This subsection describes the
376 validation of the SEBS model against heat flux measurements from a diverse range of climates.

377 In order to analyze the source of flux calculation errors, variables related to surface radiation
378 fluxes were all validated against flux station observations. Table 3 shows that H and LE have
379 RMSE values slightly less than 22 W/m^2 , which is lower than the RMSE values of products of
380 other statistical methods (see Table 7 in (Wang et al., 2007) and Table 5 in (Jiménez et al.,
381 2009)). Indeed, Kalma et al. (2008) assessed 30 published LE validation results obtained by
382 using ground flux measurements and reported an average RMSE value of about 50 W/m^2 and
383 relative errors of 15–30%. The RMSE of our LE dataset is significantly lower than their
384 averaged RMSE value.

385 We also compared our validation results with that of other, similar products produced by a
386 previous version of SEBS. Vinukollu et al. (2011b), for instance, produced global land surface
387 fluxes with RMSE values of 40.5 W/m^2 (sensible flux) and 26.1 W/m^2 (latent flux) (calculated
388 from Table 4 in (Vinukollu et al., 2011b)), which are larger than those in our study. The
389 difference could be due to the model improvement and more accurate meteorological forcing
390 dataset used in our study. Table 3 lists the values of the statistical parameters for the validation of
391 a data product produced by GLDAS (which has the highest spatial resolution compared with
392 other available terrestrial energy-flux datasets) against the same measurements from the Chinese
393 flux stations as used in our study. According to the mean values of the statistical variables, the
394 quality of our flux dataset is comparable to GLDAS' model and data assimilation results. These

395 comparisons of accuracy demonstrate that our revised model is efficient for producing a high-
396 resolution dataset of land-surface energy fluxes for China.

397 Net radiation has relatively higher RMSE and MB values than H , LE and G_0 in the dataset
398 because its accuracy is dependent on the accuracy of the other variable estimates (albedo, LST,
399 SWD, LWD, LWU, etc.). Any errors in these variables can cause bias in net radiation. LWD, for
400 example, has a linear-fitting slope value of 0.9, with most points located around the fitting line
401 (Figure 4). The correlation coefficient is as high as 0.98, thus demonstrating that there is still
402 room for improvement of the LWD algorithms. LWD in ITPCAS was calculated with algorithms
403 developed from measurements from across the Tibetan Plateau. The LWD algorithms may not,
404 therefore, be accurate for other parts of China (K. Yang, personal communication). This
405 underlines the need for more accurate LWD radiation fluxes in order to improve the accuracy of
406 turbulent fluxes and evapotranspiration.

407 In addition to the statistical evaluation of model results against observations, seasonal and inter-
408 annual changes in the model results also need to be checked. Yucheng station, which is an
409 agricultural experimental station with winter wheat and summer maize as dominant crops was
410 taken as an example (Figure 52). Crops at Yucheng station mature twice per year, which is
411 representative of warm temperate farming cropland, typical for the North China Plain. A two-
412 year flux dataset was used to compare against values extracted from our model-derived product.
413 The inter-annual and seasonal LST and LWU data closely match the in-situ observations. The
414 SWD term also successfully captures seasonal variations. LWD is systematically lower than
415 observations. The LE produced at Yucheng station not only captures seasonal variation, but also
416 responds at step stages, which occur when the wheat is harvested or maize seeds have just been

Formatted: Font: Not Italic

Formatted: Font: Not Italic

Formatted: Font: Not Italic

sown (from June to August). The increased sensible heat and decreased latent heat flux observed in July 2003 were caused by the wheat harvest, however this signal change is not captured by the model result. The simulated sensible and latent heat produced by SEBS has a one-month lag when compared to reality. This phenomenon is caused by adopting a maximum monthly NDVI value, resulting in faulty representation of canopy status changes in the month of June.

The Semi-Arid Climate and Environment Observatory of Lanzhou University (SC station) is situated on China's Loess Plateau, at 1965.8 m above sea level. Annual mean precipitation there is 381.1 mm and annual evapotranspiration is 1528.5 mm (Huang et al., 2008). Being typical of stations operating under arid conditions, its flux measurements were compared with the grid point values extracted from the model product (Figure 6-3). In 2008 the land surface around the station was covered by snow from 19 January to 20 February. Consequently the GlobAlbedo value was high for February. Unexpectedly, albedo was relatively low for January, which could be caused by the coarse temporal sampling of the station pixel by the satellite sensor. The calculated monthly sensible heat and latent heat in January 2008 have biases of -11.7 (with an observed monthly mean sensible heat = 15 W/m²) and -7.6 W/m² (with an observed monthly mean latent heat = 4.8 W/m²), respectively. The relatively large bias for SC station when covered with snow may be caused by the mixed pixel around the station.

The results of other stations have been included in supplementary materials submitted with this paper. Comparison with the results of these other stations shows that model estimates of surface energy balance variables match the magnitude and seasonal variation observed at stations in several contrasting ecosystems. Comparisons between the flux-tower-measured and the modeled fluxes show that latent fluxes were more accurate than sensible fluxes. Comparisons with other

studies, which are presented in Table 4, show that the accuracy of our dataset is one of the best among high-resolution datasets of land surface fluxes.

4.3.2 Spatial distribution of land-surface energy fluxes.

Using maps of average annual land-surface radiation and energy fluxes, we analyzed the spatial patterns of radiation and energy fluxes for the Chinese landmass and compared them with other products, such as GLDAS. The highest values of downward surface solar radiation (Figure 74a) are located in the southwest of the Tibetan Plateau, while the lowest values occur in the Sichuan Basin (SB). The highest levels of upward short-wave radiation (Figure 74c) occur around the snow-covered peaks of the Himalaya (HM), Karakorum (KRM) and Kunlun (KLM), and the Qilian (QLM) and Nyainqentanglha (NQM) mountain ranges. The strongest net solar radiation (SWD minus SWU) on the Chinese landmass occurs in the southern part of the Tibetan Plateau (see supplementary materials). The downward and upward long-wave radiation (Figures 74b and 74c) on the Tibetan Plateau are the lowest for the entire Chinese landmass. Southern China has the highest levels of upward and downward long-wave radiation. The highest values of net long-wave radiation (LWU minus LWD) occur in the southern and western parts of the Tibetan Plateau (see supplementary materials).

Figure 85 shows that northwestern China (NWC), the western Tibetan Plateau (TP), the inner Mongolian Plateau (MP) and the Loess Plateau (LP) have the highest yearly average values for surface sensible-heat flux. Croplands of the northern China Plain (NCP, including the lowlands of Shandong, Henan, and Hebei provinces) and the northeastern China Plain (NEP, including the

lowlands of Liaoning, Jilin, and Heilongjiang provinces) have low average yearly values for sensible heat flux. The Pearl River delta (PRD) and Tarim (TRB) and Sichuan (SCB) basins also have low levels of sensible heat flux, as do the Yinchuan (YCB) and the inner Mongolian basins (IMB) along the Yellow River. This spatial distribution is consistent with GLDAS results (see supplementary materials).

Simulated annual latent heat fluxes (Figure 85b) exhibit a southeast to northwest decreasing gradient, which is consistent with other studies (Liu et al., 2013c). The southeastern Tibetan Plateau has high levels of annual latent heat flux. The Gobi desert, in the northwest of China (NWC), has the lowest annual latent heat flux, followed by the western Tibetan Plateau and the inner Mongolian Plateau (MP). Lake regions along the Yangtze River and the region of basins along the Yellow River have relatively high levels of latent heat flux.

The highest levels of annual average surface net radiation (Figure 85c) can be found in southwestern China and the Lasha Basin (LB); the lowest levels occur in the Sichuan (SCB) and Junggar Basins (JB). The highest levels of annual average ground-heat flux (Figure 85c) are to be found in western China, due to large amounts of incoming solar radiation that occur under dry conditions. The monthly average of G0 is negligible when compared with other fluxes.

The role of plateau heating on Asia's monsoons is being discussed vigorously (Qiu, 2013; Wu et al., 2012; Boos and Kuang, 2010). Figure 96 shows seasonal comparisons of H between boreal winter (DJF), spring (MAM), summer (JJA) and autumn (SON). The largest area of positive sensible heating occurs in spring. Lee et al. (2011) have shown that contrasting sensible heat fluxes between the Chinese landmass and the seas surrounding it during the pre-monsoon period (April-May) affect monsoon development in East Asia. Figure 96 (a) shows that sources of

482 sensible heating in spring occur over the Tibetan and several other plateaus in China. During
483 summer, the highest sensible heat fluxes are to be found on the western Tibetan Plateau, the
484 eastern Loess Plateau (LP) and in northwestern China (NWC).

485 LE in summer has the largest area of high latent heating, followed by that in spring, autumn and
486 winter (Figure 107). Latent heat in summer is highest in southeastern and southern China as a
487 result of abundant rainfall in these regions. Similarly on irrigated land, such as that found in
488 Yinchuan (YB), the inner Mongolian basin (IMB) and the downstream basins of the Tianshan
489 (TM) and Kunlun (KLM) mountains, latent heat and evapotranspiration are high due to the
490 ample supply of water in summer. Latent heat fluxes in autumn and winter are significantly
491 lower than those of the other two seasons. The magnitudes and spatial patterns of LE in China of
492 our product are generally consistent with other reports (Yao et al., 2013; Mu et al., 2007; Jung et
493 al., 2010).

494 Net radiation in summer has the highest values of the four seasons. Most of the Chinese
495 landmass acts as a source of surface energy for the atmosphere (Figure 118).

496

497 **4.43 Trend analysis**

498 The ability to capture the inter- and intra-annual variation for each land-surface energy variable
499 is of interest to researchers of monsoon phenomena and climate change (Zhu et al., 2012). Indeed,
500 understanding these variations is essential for studies on climate change and water-resource-
501 related issues. We have calculated annual average values for each flux variable. The
502 nonparametric Mann-Kendall test (MK) is one of the most widely used methods for hydro-

meteorological time series analysis (Liu et al., 2013d;Gan, 1998). The MK method was applied to the series of annual average fluxes to check variations during the period 2001–2010. The resulting slope indicates that downward surface short-wave radiation increased during that decade over the majority of the Tibetan Plateau (Figure 129).

The ground solar measurements at China Meteorological Administration (CMA) stations during 2003–2006, as shown in Figure 1b of Yang et al. (2012), confirms the increasing trend of downward surface short-wave radiation found in our study. The annual mean visibility measured at these stations also displays an increasing trend (Figure 2a of Yang et al. (2012)), while ERA-40 reanalyzed precipitable-water and station-observed specific humidity show a decreasing trend from 2000 to 2006 (Figure3a of Yang et al. (2012)). These results indicate that the atmosphere over the plateau is becoming drier, which would explain why SWD has increased during the decade.

The upward short-wave radiation over the Himalaya (HM), the Ganges (GM), the Karakorum (KRM), and the Qilian (QLM) and Nyainqentanglha (NQM) mountain ranges has also increased over the last 10 years, which may be caused by the glacial retreat that has occurred in these areas (Scherler et al., 2011;Yao et al., 2004). Lasha basin (LB) has the steepest rising trend in LWU, perhaps because of the relatively greater degree of anthropogenic (e.g. urbanization) activity occurring in this area. The trend analysis did not reveal any clear spatial pattern in downward long-wave radiation. Net radiation over several high mountain ranges (including the Himalaya, the Ganges, the Karakorum and the Qilian and Nyainqentanglha mountain ranges) increased by approximately 5 W/m² between 2001 and 2010 (Figure 130). The strongest increase in net radiation occurred in the central part of the Tibetan Plateau. As Matthew (2010) has pointed out,

525 soil moisture in the central Tibetan Plateau showed an increasing trend from 1987 to 2008.
526 Wetter soil can cause the ground surface to absorb more net radiation and thus increase latent
527 heat flux. Moreover, wetter soil can increase soil heating capacity (Guan et al., 2009) and so
528 further increase ground heat flux. The increases in net radiation and soil moisture may also
529 explain a rising trend in latent heat in the central Tibetan Plateau. Clearly, the plateau is
530 experiencing accelerated environmental changes (Zhong et al., 2011; Salama et al., 2012). Indeed,
531 land-surface radiation and energy trend analyses also show that the Tibetan Plateau is
532 experiencing a relatively stronger change in land-surface radiation (verified by Tang et al. (2011)
533 and energy exchange than other parts of China.

534

535 5 Conclusions and discussion

536 In view of China's highly fragmented landscape, high-resolution land-surface heat flux maps are
537 necessary for hydrological studies. As China includes arid, semi-arid, humid, and semi-humid
538 regions, quantifying its water and energy budgets is a challenge. We have developed the surface
539 energy balance system (SEBS) further to produce a land-surface heat flux dataset at a continental
540 scale of higher resolution than datasets derived using other methods. Generally, the global
541 surface energy flux data sets, including reanalysis data, do not have enough spatial and temporal
542 resolution when looking at the national-level fluxes. The surface flux data sets from reanalysis
543 data sets still contain large uncertainty, partly due to the deficiency in their land surface process
544 model that simulate land surface temperature by solving soil thermal transport equations (Chen
545 et al., 1996) and usually result in a large error in LST simulation (Chen et al., 2011; Wang et al.,
546 2014) if the model is not properly calibrated by measurements (Hogue et al., 2005). So the

Formatted: Font: (Default) Times New Roman, Not Italic

Formatted: Font: (Default) Times New Roman, Not Italic

Formatted: Font: (Default) Times New Roman, Not Italic

Formatted: Font: (Default) Times New Roman, Not Italic

Formatted: Font: (Default) Times New Roman, Not Italic

Formatted: Font: (Default) Times New Roman, Not Italic

Formatted: Font: (Default) Times New Roman, Not Italic

Formatted: Font: (Default) Times New Roman, Not Italic

547 hypothesis tested in this paper is if it is possible to neglect the complex process in the soil by
548 using satellite observed land surface temperature directly to calculate the land surface fluxes at
549 continental scale? This study has demonstrated a benchmark on how to use satellite to derive a
550 land surface flux dataset for a continental area on a personal laptop which is absolutely not
551 feasible for the land surface process modeler to do in such a time and resource economic way.
552 We have overcome the shortages of previous remotely-sensed evapotranspiration products which
553 have null values in barren and desert areas. We also found a solution on how to produce a
554 dynamic surface roughness length due to variations in the canopy height, which is closer to the
555 reality, for a continental area. Usually, the surface roughness length is given a fixed value in
556 numerical models. In summary, using remote sensing data and surface meteorological
557 information, an independent data product of monthly resolution has been developed for land-
558 surface heat flux analysis. We have validated our remote-sensing-based approach with in-situ
559 observations from 11 flux stations in China. Taking into account the limitations of available
560 spatial data and computing resources, we applied the model to the entire Chinese landmass using
561 a 0.1-degree resolution meteorological dataset, MODIS LST, vegetation indices and other
562 variables to generate a climatological dataset of land-surface energy balance for a 10-year period.
563 The modeling results for both pixel-point and spatial distribution demonstrate that this approach
564 meets our aims in terms of (a) being robust across a variety of land cover and climate types and
565 (b) performing well for the temporal and spatial scales of interest. The spatial distribution maps
566 generated for each variable of surface energy balance give important background information on
567 the terrestrial hydrology and energy cycles. This product also demonstrates the impact of
568 topography and climatic conditions on land–air energy and moisture exchanges in China.

Formatted: Font: (Default) Times New Roman, Not Italic

Formatted: Font: (Default) Times New Roman, Not Italic

Formatted: Font: (Default) Times New Roman, Not Italic

Formatted: Font: (Default) Times New Roman, Not Italic

Formatted: Font: Not Italic

Formatted: Font: Not Italic

Formatted: Font: Not Italic

Formatted: Font: Not Italic

Formatted: Font: Not Italic

Formatted: Font: (Default) Times New Roman, Not Italic

569 The applicability of remote-sensing-based estimates of land surface fluxes is hampered by
570 limited temporal coverage of satellite sensors (Ryu et al., 2012). Remote sensing data are
571 snapshots of the land surface status at a particular point in space and time (Ryu et al., 2011). It is
572 challenging to compare remote-sensing-based monthly flux data with ground measurements that
573 are made on time scales ranging from half-hourly through to monthly. The accuracy of land
574 surface heat fluxes is largely dependent on the remotely sensed land surface temperature. Here
575 we have made an assumption that the averaged Aqua and Terra sensors sensed LST in each
576 month can represent the monthly average LST. Terra satellite sensor passes twice a day (at about
577 10:30am, and 22:30pm local time), also the Aqua satellite passes twice a day (at about 01:30am,
578 and 13:30pm local time). So MODIS have four samples each day. The samples may not be
579 enough for calculating the monthly LST, also due to the cloud noise. Besides, the time period of
580 MODIS datasets is not longer than 15 years which may limit application of our dataset in climate
581 analysis. Additionally, the sensible heat flux over forest is underestimated by present turbulent
582 flux parameterization method in SEBS which does not take the roughness sublayer over high
583 canopy (Bosveld, 1999) into consideration.

Formatted: Font: Not Bold

Formatted: Font: Not Bold

584 The energy flux product we have developed has a spatial resolution of approximately 10 km,
585 while flux towers have a footprint of tens to hundreds of meters. The tower footprint may not be
586 representative of the larger pixel of the product, and this mismatch will result in errors if the
587 mean of the satellite pixel is different from that of the flux tower footprint. Remote-sensing-
588 based studies stress that direct comparison is a challenge because scale mismatch (Norman et al.,
589 2003) and heterogeneity of the land surface reduce the spatial representativeness of ground-site
590 measurements (Mi et al., 2006). Another challenge is validating the grid-box-based simulation

results on the scale of the Chinese landmass, since reliable observations of flux data are only available from a few sites in the simulated region.

Potential effects of changes in ~~turbulent~~land surface heat fluxes on the monsoon over East Asia (Lee et al., 2011) as a result of China's recent urbanization can be studied further using our product. As an independent satellite-based product, it can also be used as a data source for evaluating land surface models. We also produced a evapotranspiration product for China land area using the dataset in this paper. The land surface fluxes and evapotranspiration product can be downloaded from the URL. Recent result will be shared when the forcing dataset is available:
<https://drive.google.com/folderview?id=0B7yGrB1U9eDec2JFbnA5eldlVHc&usp=sharing>

Acknowledgements

This study was supported by the Chinese National Key Program for Developing Basic Sciences (2010CB951701), the Chinese National Natural Science Foundation (41275010), CAS-KNAW joint PhD project, the ESA WACMOS project and the FP7 CORE-CLIMAX project. The forcing dataset used in our study was developed at the Data Assimilation and Modeling Center for Tibetan Multi-spheres, Institute of Tibetan Plateau Research, Chinese Academy of Sciences. We thank Professor Yang Kun for his comments during the writing of this paper. For our study we used eddy covariance data acquired from the scientific community and networks. We

611 acknowledge Wenjiang, Ali, Yucheng, and Weishan stations,
612 Nagqu Station of Plateau Climate and Environment, Magqu Zoige Plateau Wetlands Ecosystem
613 Research Station, and the Semi-Arid Climate and Environment Observatory of Lanzhou
614 University for providing their in-situ measurement datasets. We also acknowledge Professor
615 Xiangde Xu (CMA), Dr. Lide Tian (ITP, CAS), Dr. Yu Zhang (CAREERI, CAS), Dr. Shouhua
616 Xu (IGSNRR, CAS), Dr. Bin Zhao (Fudan University), and Dr. Huimin Lei (Tsinghua University)
617 for providing us with their flux datasets.

618

619

620

621

622

623

624

625

626

627

628

629

631 **References**

- 632 Allen, R., Irmak, A., Trezza, R., Hendrickx, J. M. H., Bastiaanssen, W., and Kjaersgaard, J.: Satellite-based
 633 ET estimation in agriculture using SEBAL and METRIC, *Hydrol Process*, 25, 4011-4027, 10.1002/hyp.8408,
 634 2011.
- 635 Boos, W. R., and Kuang, Z.: Dominant control of the South Asian monsoon by orographic insulation
 636 versus plateau heating, *Nature*, 463, 218-222, 10.1038/nature08707, 2010.
- 637 Bosveld, F. C.: Exchange processes between a coniferous forest and the atmosphere, Ph.D, Wageningen
 638 University, 181 pp., 1999.
- 639 Brauman, K., Daily, G., Duarte, T., and Mooney, H.: The nature and value of ecosystem services: An
 640 overview highlighting hydrologic services, in: *Annual Review of Environment and Resources*, Annual
 641 Review of Environment and Resources, Annual Reviews, Palo Alto, 67-98, 2007.
- 642 Brutsaert, W.: Aspects of bulk atmospheric boundary layer similarity under free-convective conditions,
 643 *Rev. Geophys.*, 37, 439-451, 10.1029/1999rg900013, 1999.
- 644 Cammalleri, C., Anderson, M. C., Ciraolo, G., D'Urso, G., Kustas, W. P., La Loggia, G., and Minacapilli, M.:
 645 The impact of in-canopy wind profile formulations on heat flux estimation in an open orchard using the
 646 remote sensing-based two-source model, *Hydrol. Earth Syst. Sci.*, 14, 2643-2659, 10.5194/hess-14-2643-
 647 2010, 2010.
- 648 Chen, F., Mitchell, K., Schaake, J., Xue, Y., Pan, H.-L., Koren, V., Duan, Q. Y., Ek, M., and Betts, A.:
 649 Modeling of land surface evaporation by four schemes and comparison with FIFE observations, *Journal*
 650 *of Geophysical Research: Atmospheres*, 101, 7251-7268, 10.1029/95jd02165, 1996.
- 651 Chen, J., Jönsson, P., Tamura, M., Gu, Z., Matsushita, B., and Eklundh, L.: A simple method for
 652 reconstructing a high-quality NDVI time-series data set based on the Savitzky–Golay filter, *Remote*
 653 *Sensing of Environment*, 91, 332-344, <http://dx.doi.org/10.1016/j.rse.2004.03.014>, 2004.
- 654 Chen, X., Su, Z., Ma, Y., Yang, K., and Wang, B.: Estimation of surface energy fluxes under complex
 655 terrain of Mt. Qomolangma over the Tibetan Plateau, *Hydrol. Earth Syst. Sci.*, 17, 1607-1618,
 656 10.5194/hess-17-1607-2013, 2013a.
- 657 Chen, X., Su, Z., Ma, Y., Yang, K., Wen, J., and Zhang, Y.: An Improvement of Roughness Height
 658 Parameterization of the Surface Energy Balance System (SEBS) over the Tibetan Plateau, *J. Appl.*
 659 *Meteorol. Climatol.*, 52, 607-622, 10.1175/jamc-d-12-056.1, 2013b.
- 660 Chen, Y., Yang, K., He, J., Qin, J., Shi, J., Du, J., and He, Q.: Improving land surface temperature modeling
 661 for dry land of China, *J. Geophys. Res.*, 116, D20104, 10.1029/2011jd015921, 2011.
- 662 Chen, Y., Yang, K., Qin, J., Zhao, L., Tang, W., and Han, M.: Evaluation of AMSR-E retrievals and GLDAS
 663 simulations against observations of a soil moisture network on the central Tibetan Plateau, *Journal of*
 664 *Geophysical Research: Atmospheres*, 118, 4466-4475, 10.1002/jgrd.50301, 2013c.
- 665 Coll, C., Wan, Z., and Galve, J. M.: Temperature-based and radiance-based validations of the V5 MODIS
 666 land surface temperature product, *J. Geophys. Res.*, 114, D20102, 10.1029/2009jd012038, 2009.
- 667 Decker, M., Brunke, M. A., Wang, Z., Sakaguchi, K., Zeng, X., and Bosilovich, M. G.: Evaluation of the
 668 Reanalysis Products from GSFC, NCEP, and ECMWF Using Flux Tower Observations, *Journal of Climate*,
 669 25, 1916-1944, 10.1175/jcli-d-11-00004.1, 2011.
- 670 Dee, D. P., Uppala, S. M., Simmons, A. J., Berrisford, P., Poli, P., Kobayashi, S., Andrae, U., Balmaseda, M.
 671 A., Balsamo, G., Bauer, P., Bechtold, P., Beljaars, A. C. M., van de Berg, L., Bidlot, J., Bormann, N., Delsol,
 672 C., Dragani, R., Fuentes, M., Geer, A. J., Haimberger, L., Healy, S. B., Hersbach, H., Hólm, E. V., Isaksen, L.,

Källberg, P., Köhler, M., Matricardi, M., McNally, A. P., Monge-Sanz, B. M., Morcrette, J. J., Park, B. K.,
 Peubey, C., de Rosnay, P., Tavolato, C., Thépaut, J. N., and Vitart, F.: The ERA-Interim reanalysis:
 configuration and performance of the data assimilation system, *Quarterly Journal of the Royal
 Meteorological Society*, 137, 553-597, 10.1002/qj.828, 2011.
 Dirmeyer, P. A., Gao, X., Zhao, M., Guo, Z., Oki, T., and Hanasaki, N.: GSWP-2: Multimodel Analysis and
 Implications for Our Perception of the Land Surface, *Bulletin of the American Meteorological Society*, 87,
 1381-1397, 10.1175/bams-87-10-1381, 2006.
 Fan, L., Liu, S., Bernhofer, C., Liu, H., and Berger, F. H.: Regional land surface energy fluxes by satellite
 remote sensing in the Upper Xilin River Watershed (Inner Mongolia, China), *Theoretical and Applied
 Climatology*, 88, 231-245, 10.1007/s00704-006-0241-9, 2007.
 Fisher, J. B., Tu, K. P., and Baldocchi, D. D.: Global estimates of the land-atmosphere water flux based on
 monthly AVHRR and ISLSCP-II data, validated at 16 FLUXNET sites, *Remote Sensing of Environment*, 112,
 901-919, <http://dx.doi.org/10.1016/j.rse.2007.06.025>, 2008.
 Flerchinger, G., Xiao, W., Marks, D., Sauer, T., and Yu, Q.: Comparison of algorithms for incoming
 atmospheric long-wave radiation, *Water Resour. Res.*, 45, W03423, 10.1029/2008wr007394, 2009.
 Gan, T. Y.: Hydroclimatic trends and possible climatic warming in the Canadian Prairies, *Water Resources
 Research*, 34, 3009-3015, 10.1029/98wr01265, 1998.
 Goudriaan, J.: Crop micrometeorology: a simulation study, PhD thesis, Wageningen University 249 pp.,
 1977.
 Guan, X., Huang, J., Guo, N., Bi, J., and Wang, G.: Variability of soil moisture and its relationship with
 surface albedo and soil thermal parameters over the Loess Plateau, *Advances in Atmospheric Sciences*,
 26, 692-700, 10.1007/s00376-009-8198-0, 2009.
 He, J.: Development of surface meteorological dataset of China with high temporal and spatial
 resolution, M.S. Inst. of Tibetan Plateau Res., Chin. Acad. of Sci., Beijing, China, 2010.
 Hogue, T. S., Bastidas, L., Gupta, H., Sorooshian, S., Mitchell, K., and Emmerich, W.: Evaluation and
 Transferability of the Noah Land Surface Model in Semiarid Environments, *Journal of Hydrometeorology*,
 6, 68-84, 10.1175/jhm-402.1, 2005.
 Hsu, H.-H., and Liu, X.: Relationship between the Tibetan Plateau heating and East Asian summer
 monsoon rainfall, *Geophys. Res. Lett.*, 30, 2066, 10.1029/2003gl017909, 2003.
 Huang, J., Zhang, W., Zuo, J., Bi, J., Shi, J., Wang, X., Chang, Z., Huang, Z., Yang, S., Zhang, B., Wang, G.,
 Feng, G., Yuan, J., Zhang, L., Zuo, H., Wang, S., Fu, C., and Jifan, C.: An overview of the semi-arid climate
 and environment research observatory over the Loess Plateau, *Adv. Atmos. Sci.*, 25, 906-921, 2008.
 Jia, Z., Liu, S., Xu, Z., Chen, Y., and Zhu, M.: Validation of remotely sensed evapotranspiration over the
 Hai River Basin, China, *J. Geophys. Res.*, 117, D13113, 10.1029/2011jd017037, 2012.
 Jiménez, C., Prigent, C., and Aires, F.: Toward an estimation of global land surface heat fluxes from
 multisatellite observations, *J. Geophys. Res.*, 114, D06305, 10.1029/2008jd011392, 2009.
 Jiménez, C., Prigent, C., Mueller, B., Seneviratne, S. I., McCabe, M. F., Wood, E. F., Rossow, W. B.,
 Balsamo, G., Betts, A. K., Dirmeyer, P. A., Fisher, J. B., Jung, M., Kanamitsu, M., Reichle, R. H., Reichstein,
 M., Rodell, M., Sheffield, J., Tu, K., and Wang, K.: Global intercomparison of 12 land surface heat flux
 estimates, *J. Geophys. Res.*, 116, D02102, 10.1029/2010jd014545, 2011.
 Jung, M., Reichstein, M., and Bondeau, A.: Towards global empirical upscaling of FLUXNET eddy
 covariance observations: validation of a model tree ensemble approach using a biosphere model,
Biogeosciences, 6, 2001-2013, 10.5194/bg-6-2001-2009, 2009.
 Jung, M., Reichstein, M., Ciais, P., Seneviratne, S. I., Sheffield, J., Goulden, M. L., Bonan, G., Cescatti, A.,
 Chen, J., de Jeu, R., Dolman, A. J., Eugster, W., Gerten, D., Gianelle, D., Gobron, N., Heinke, J., Kimball, J.,
 Law, B. E., Montagnani, L., Mu, Q., Mueller, B., Oleson, K., Papale, D., Richardson, A. D., Rouspard, O.,
 Running, S., Tomelleri, E., Viovy, N., Weber, U., Williams, C., Wood, E., Zaehle, S., and Zhang, K.: Recent

decline in the global land evapotranspiration trend due to limited moisture supply, *Nature*, 467, 951-954, <http://www.nature.com/nature/journal/v467/n7318/abs/nature09396.html#supplementary-information>, 2010.

Jung, M., Reichstein, M., Margolis, H. A., Cescatti, A., Richardson, A. D., Arain, M. A., Arneth, A., Bernhofer, C., Bonal, D., Chen, J., Gianelle, D., Gobron, N., Kiely, G., Kutsch, W., Lasslop, G., Law, B. E., Lindroth, A., Merbold, L., Montagnani, L., Moors, E. J., Papale, D., Sottocornola, M., Vaccari, F., and Williams, C.: Global patterns of land-atmosphere fluxes of carbon dioxide, latent heat, and sensible heat derived from eddy covariance, satellite, and meteorological observations, *J. Geophys. Res.*, 116, G00J07, 10.1029/2010jg001566, 2011.

Kalma, J., McVicar, T., and McCabe, M.: Estimating land surface evaporation: a review of methods using remotely sensed surface temperature data, *Surveys in Geophysics*, 29, 421-469, 10.1007/s10712-008-9037-z, 2008.

Kalnay, E., Kanamitsu, M., Kistler, R., Collins, W., Deaven, D., Gandin, L., Iredell, M., Saha, S., White, G., Woollen, J., Zhu, Y., Leetmaa, A., Reynolds, R., Chelliah, M., Ebisuzaki, W., Higgins, W., Janowiak, J., Mo, K. C., Ropelewski, C., Wang, J., Jenne, R., and Joseph, D.: The NCEP/NCAR 40-year reanalysis project, *Bulletin of the American Meteorological Society*, 77, 437-471, 10.1175/1520-0477(1996)077<0437:tnyrp>2.0.co;2, 1996.

Lee, E., Barford, C., Kucharik, C., Felzer, B., and Foley, J.: Role of turbulent heat fluxes over land in the monsoon over East Asia, *International Journal of Geosciences*, 2 420-431, 10.4236/ijg.2011.24046., 2011.

Lei, H., and Yang, D.: Interannual and seasonal variability in evapotranspiration and energy partitioning over an irrigated cropland in the North China Plain, *Agricultural and Forest Meteorology*, 150, 581-589, <http://dx.doi.org/10.1016/j.agrformet.2010.01.022>, 2010a.

Lei, H., and Yang, D.: Seasonal and interannual variations in carbon dioxide exchange over a cropland in the North China Plain, *Global Change Biology*, 16, 2944-2957, 10.1111/j.1365-2486.2009.02136.x, 2010b.

Li, X., Li, X., Li, Z., Ma, M., Wang, J., Xiao, Q., Liu, Q., Che, T., Chen, E., Yan, G., Hu, Z., Zhang, L., Chu, R., Su, P., Liu, Q., Liu, S., Wang, J., Niu, Z., Chen, Y., Jin, R., Wang, W., Ran, Y., Xin, X., and Ren, H.: Watershed Allied Telemetry Experimental Research, *Journal of Geophysical Research: Atmospheres*, 114, D22103, 10.1029/2008jd011590, 2009.

Li, X., Liang, S., Yuan, W., Yu, G., Cheng, X., Chen, Y., Zhao, T., Feng, J., Ma, Z., Ma, M., Liu, S., Chen, J., Shao, C., Li, S., Zhang, X., Zhang, Z., Sun, G., Chen, S., Ohta, T., Varlagin, A., Miyata, A., Takagi, K., Saikusa, N., and Kato, T.: Estimation of evapotranspiration over the terrestrial ecosystems in China, *Ecohydrology*, 7, 139-149, 10.1002/eco.1341, 2012a.

Li, X., Wang, L., Chen, D., Yang, K., Xue, B., and Sun, L.: Near-surface air temperature lapse rates in the mainland China during 1962–2011, *Journal of Geophysical Research: Atmospheres*, 118, 7505-7515, 10.1002/jgrd.50553, 2013.

Li, Z., Zheng, F.-L., and Liu, W.-Z.: Spatiotemporal characteristics of reference evapotranspiration during 1961–2009 and its projected changes during 2011–2099 on the Loess Plateau of China, *Agricultural and Forest Meteorology*, 154–155, 147-155, 10.1016/j.agrformet.2011.10.019, 2012b.

Lin, W., Zhang, L., Du, D., Yang, L., Lin, H., Zhang, Y., and Li, J.: Quantification of land use/land cover changes in Pearl River Delta and its impact on regional climate in summer using numerical modeling, *Reg Environ Change*, 9, 75-82, 10.1007/s10113-008-0057-5, 2009.

Liu, J., and Xie, Z.: Improving simulation of soil moisture in China using a multiple meteorological forcing ensemble approach, *Hydrol. Earth Syst. Sci.*, 17, 3355-3369, 10.5194/hess-17-3355-2013, 2013.

Liu, N., Liu, Q., Wang, L., Liang, S., Wen, J., Qu, Y., and Liu, S.: A statistics-based temporal filter algorithm to map spatiotemporally continuous shortwave albedo from MODIS data, *Hydrol. Earth Syst. Sci.*, 17, 10.5194/hess-17-2121-2013, 2013a.

766 Liu, R., Wen, J., Wang, X., Wang, L., Tian, H., Zhang, T. T., Shi, X. K., Zhang, J. H., and Lv, S. N.: Actual daily
 767 evapotranspiration estimated from MERIS and AATSR data over the Chinese Loess Plateau, *Hydrol. Earth*
 768 *Syst. Sci.*, 14, 47-58, 10.5194/hess-14-47-2010, 2010.
 769 Liu, S., Xu, Z., Wang, W., Jia, Z., Zhu, M., Bai, J., and Wang, J.: A comparison of eddy-covariance and large
 770 aperture scintillometer measurements with respect to the energy balance closure problem, *Hydrol.*
 771 *Earth Syst. Sci.*, 15, 1291-1306, 10.5194/hess-15-1291-2011, 2011.
 772 Liu, S. M., Xu, Z. W., Zhu, Z. L., Jia, Z. Z., and Zhu, M. J.: Measurements of evapotranspiration from eddy-
 773 covariance systems and large aperture scintillometers in the Hai River Basin, China, *Journal of Hydrology*,
 774 487, 24-38, 10.1016/j.jhydrol.2013.02.025,, 2013b.
 775 Liu, Y., Zhou, Y., Ju, W., Chen, J., Wang, S., He, H., Wang, H., Guan, D., Zhao, F., Li, Y., and Hao, Y.:
 776 Changes of evapotranspiration and water yield in China's terrestrial ecosystems during the period from
 777 2000 to 2010, *Hydrol. Earth Syst. Sci.*, 17, 2121-2129, 10.5194/hessd-10-5397-2013, 2013c.
 778 Liu, Z., Zhou, P., Zhang, F., Liu, X., and Chen, G.: Spatiotemporal characteristics of dryness/wetness
 779 conditions across Qinghai Province, Northwest China, *Agricultural and Forest Meteorology*, 182-183,
 780 <http://dx.doi.org/10.1016/j.agrformet.2013.05.013>, 2013d.
 781 Ma, L., Zhang, T., Li, Q., Frauenfeld, O. W., and Qin, D.: Evaluation of ERA-40, NCEP-1, and NCEP-2
 782 reanalysis air temperatures with ground-based measurements in China, *J. Geophys. Res.*, 113, D15115,
 783 10.1029/2007jd009549, 2008a.
 784 Ma, Y., Su, Z., Li, Z., Koike, T., and Menenti, M.: Determination of regional net radiation and soil heat flux
 785 over a heterogeneous landscape of the Tibetan Plateau, *Hydrological Processes*, 16, 2963-2971, 2002.
 786 Ma, Y., Zhong, L., Su, Z., Ishikawa, H., Menenti, M., and Koike, T.: Determination of regional distributions
 787 and seasonal variations of land surface heat fluxes from Landsat-7 Enhanced Thematic Mapper data
 788 over the central Tibetan Plateau area, *J. Geophys. Res.*, 111, D10305, 10.1029/2005jd006742, 2006.
 789 Ma, Y., Zhong, L., Wang, B., Ma, W., Chen, X., and Li, M.: Determination of land surface heat fluxes over
 790 heterogeneous landscape of the Tibetan Plateau by using the MODIS and in situ data, *Atmos. Chem.*
 791 *Phys.*, 11, 10461-10469, 10.5194/acp-11-10461-2011, 2011.
 792 Ma, Y., Kang, S., Zhu, L., Xu, B., Tian, L., and Yao, T.: Tibetan Observation and Research Platform-
 793 Atmosphere-land interaction over a heterogeneous landscape, *Bull. Amer. Meteor. Soc.*, 89, 1487-1492,
 794 10.1175/2008BAMS2545.1, 2008b.
 795 Massman, W. J.: An analytical one-dimensional second-order closure model of turbulence statistics and
 796 the lagrangian time scale within and above plant canopies of arbitrary structure, *Boundary Layer*
 797 *Meteorology*, 83, 407-421, 1997.
 798 Matthew, O.: Characterization of the effects of climate variation on land surface temperature and soil
 799 moisture through stochastic analysis of long term SSM/I observations over the Tibetan plateau, Master,
 800 International Institute for Geo-information Science and Earth Observation, University of Twente,
 801 Enschede, The Netherlands, 1-67 pp., 2010.
 802 Meir, P., and Woodward, F. I.: Amazonian rain forests and drought: response and vulnerability, *New*
 803 *Phytologist*, 187, 553-557, 10.1111/j.1469-8137.2010.03390.x, 2010.
 804 Mi, N., Yu, G. R., Wang, P. X., Wen, X. F., and Sun, X. M.: A preliminary study for spatial representiveness
 805 of flux observation at ChinaFLUX sites, *Science in China Series D-Earth Sciences*, 49, 24-35,
 806 10.1007/s11430-006-8024-9|ISSN 1006-9313, 2006.
 807 Moody, E. G., King, M. D., Platnick, S., Schaaf, C. B., and Feng, G.: Spatially complete global spectral
 808 surface albedos: value-added datasets derived from Terra MODIS land products, *Geoscience and*
 809 *Remote Sensing, IEEE Transactions on*, 43, 144-158, 10.1109/tgrs.2004.838359, 2005.
 810 Mu, Q., Heinsch, F. A., Zhao, M., and Running, S. W.: Development of a global evapotranspiration
 811 algorithm based on MODIS and global meteorology data, *Remote Sensing of Environment*, 111, 519-536,
 812 10.1016/j.rse.2007.04.015, 2007.

813 Mueller, B., Seneviratne, S. I., Jimenez, C., Corti, T., Hirschi, M., Balsamo, G., Ciais, P., Dirmeyer, P., Fisher,
814 J. B., Guo, Z., Jung, M., Maignan, F., McCabe, M. F., Reichle, R., Reichstein, M., Rodell, M., Sheffield, J.,
815 Teuling, A. J., Wang, K., Wood, E. F., and Zhang, Y.: Evaluation of global observations-based
816 evapotranspiration datasets and IPCC AR4 simulations, *Geophys. Res. Lett.*, 38, L06402,
817 10.1029/2010gl046230, 2011.

818 Muller, J.-P., López, G., Watson, G., Shane, N., Kennedy, T., Yuen, P., Lewis, P., Fischer, J., Guanter, L.,
819 Domench, C., Preusker, R., North, P., Heckel, A., Danne, O., and Krämer, U.: The ESA GlobAlbedo Project
820 for mapping the Earth's land surface albedo for 15 Years from European Sensors., *IEEE Geoscience and*
821 *Remote Sensing Symposium (IGARSS)*, IEEE, , Munich, Germany, , 2012.

822 Norman, J. M., Anderson, M. C., Kustas, W. P., French, A. N., Mecikalski, J., Torn, R., Diak, G. R.,
823 Schmugge, T. J., and Tanner, B. C. W.: Remote sensing of surface energy fluxes at 101-m pixel
824 resolutions, *Water Resources Research*, 39, 1221, 10.1029/2002wr001775, 2003.

825 Piao, S., Mohammat, A., Fang, J., Cai, Q., and Feng, J.: NDVI-based increase in growth of temperate
826 grasslands and its responses to climate changes in China, *Global Environmental Change*, 16, 340-348,
827 <http://dx.doi.org/10.1016/j.gloenvcha.2006.02.002>, 2006.

828 Qiu, J.: Monsoon Melee, *Science*, 340, 1400-1401, 10.1126/science.340.6139.1400, 2013.

829 Rienecker, M. M., Suarez, M. J., Gelaro, R., Todling, R., Bacmeister, J., Liu, E., Bosilovich, M. G., Schubert,
830 S. D., Takacs, L., Kim, G.-K., Bloom, S., Chen, J., Collins, D., Conaty, A., da Silva, A., Gu, W., Joiner, J.,
831 Koster, R. D., Lucchesi, R., Molod, A., Owens, T., Pawson, S., Pegion, P., Redder, C. R., Reichle, R.,
832 Robertson, F. R., Ruddick, A. G., Sienkiewicz, M., and Woollen, J.: MERRA: NASA's Modern-Era
833 Retrospective Analysis for Research and Applications, *Journal of Climate*, 24, 3624-3648, 10.1175/jcli-d-
834 11-00015.1, 2011.

835 Riihel, A., Manninen, T., Laine, V., Andersson, K., and Kaspar, F.: CLARA-SAL: a global 28-yr timeseries of
836 Earth's black-sky surface albedo, *Atmos. Chem. Phys.*, 13, 3743-3762, 10.5194/acp-13-3743-2013, 2013.

837 Roads, J., and Betts, A.: NCEP–NCAR and ECMWF reanalysis surface water and energy budgets for the
838 Mississippi River Basin, *Journal of Hydrometeorology*, 1, 88-94, 10.1175/1525-
839 7541(2000)001<0088:nnaers>2.0.co;2, 2000.

840 Rodell, M., Houser, P. R., Jambor, U., Gottschalck, J., Mitchell, K., Meng, C. J., Arsenault, K., Cosgrove, B.,
841 Radakovich, J., Bosilovich, M., Entin, J. K., Walker, J. P., Lohmann, D., and Toll, D.: The Global Land Data
842 Assimilation System, *Bulletin of the American Meteorological Society*, 85, 381-394, 10.1175/bams-85-3-
843 381, 2004.

844 Ryu, Y., Baldocchi, D. D., Kobayashi, H., van Ingen, C., Li, J., Black, T. A., Beringer, J., van Gorsel, E., Knohl,
845 A., Law, B. E., and Rouspard, O.: Integration of MODIS land and atmosphere products with a coupled-
846 process model to estimate gross primary productivity and evapotranspiration from 1 km to global scales,
847 *Global Biogeochemical Cycles*, 25, GB4017, 10.1029/2011gb004053, 2011.

848 Ryu, Y., Baldocchi, D. D., Black, T. A., Detto, M., Law, B. E., Leuning, R., Miyata, A., Reichstein, M., Vargas,
849 R., Ammann, C., Beringer, J., Flanagan, L. B., Gu, L., Hutley, L. B., Kim, J., McCaughey, H., Moors, E. J.,
850 Rambal, S., and Vesala, T.: On the temporal upscaling of evapotranspiration from instantaneous remote
851 sensing measurements to 8-day mean daily-sums, *Agricultural and Forest Meteorology*, 152, 212-222,
852 <http://dx.doi.org/10.1016/j.agrformet.2011.09.010>, 2012.

853 Salama, M. S., Velde, R., Zhong, L., Ma, Y., Ofwono, M., and Su, Z.: Decadal variations of land surface
854 temperature anomalies observed over the Tibetan Plateau by the Special Sensor Microwave Imager
855 (SSM/I) from 1987 to 2008, *Climatic Change*, 114, 769-781, 10.1007/s10584-012-0427-3, 2012.

856 Scherler, D., Bookhagen, B., and Strecker, M. R.: Spatially variable response of Himalayan glaciers to
857 climate change affected by debris cover, *Nature Geosci.*, 4, 156-159,
858 <http://www.nature.com/ngEO/journal/v4/n3/abs/ngEO1068.html#supplementary-information>, 2011.

859 Sheffield, J., Goteti, G., and Wood, E. F.: Development of a 50-Year high-resolution global dataset of
860 meteorological forcings for land surface modeling, *Journal of Climate*, 19, 3088-3111, 10.1175/jcli3790.1,
861 2006.

862 Shu, Y., Stisen, S., Jensen, K. H., and Sandholt, I.: Estimation of regional evapotranspiration over the
863 North China Plain using geostationary satellite data, *International Journal of Applied Earth Observation*
864 and *Geoinformation*, 13, 192-206, 10.1016/j.jag.2010.11.002, 2011.

865 Simard, M., Pinto, N., Fisher, J. B., and Baccini, A.: Mapping forest canopy height globally with
866 spaceborne lidar, *J. Geophys. Res.*, 116, G04021, 10.1029/2011jg001708, 2011.

867 Su, Z., Schmugge, T., Kustas, W. P., and Massman, W. J.: An evaluation of two models for estimation of
868 the roughness height for heat transfer between the land surface and the atmosphere, *Journal of Applied*
869 *Meteorology*, 40, 1933-1951, 2001.

870 Su, Z.: The Surface Energy Balance System(SEBS) for estimation of turbulent heat fluxes, *Hydrology and*
871 *Earth System Sciences*, 6, 85-99, 2002.

872 Su, Z., de Rosnay, P., Wen, J., Wang, L., and Zeng, Y.: Evaluation of ECMWF's soil moisture analyses using
873 observations on the Tibetan Plateau, *Journal of Geophysical Research: Atmospheres*, 118, 5304-5318,
874 10.1002/jgrd.50468, 2013.

875 Suh, M.-S., and Lee, D.-K.: Impacts of land use/cover changes on surface climate over east Asia for
876 extreme climate cases using RegCM2, *Journal of Geophysical Research: Atmospheres*, 109, D02108,
877 10.1029/2003jd003681, 2004.

878 Sun, L., and Wu, G.: Influence of land evapotranspiration on climate variations, *Science in China Series D:*
879 *Earth Sciences*, 44, 838-846, 10.1007/bf02907096, 2001.

880 Tang, W. J., Yang, K., Qin, J., Cheng, C. C. K., and He, J.: Solar radiation trend across China in recent
881 decades: a revisit with quality-controlled data, *Atmos. Chem. Phys.*, 11, 393-406, 10.5194/acp-11-393-
882 2011, 2011.

883 Taniguchi, K., and Koike, T.: Seasonal variation of cloud activity and atmospheric profiles over the
884 eastern part of the Tibetan Plateau, *J. Geophys. Res.-Atmos.*, 113, 10104-10104, 2008.

885 Timmermans, J.: Coupling optical and thermal directional radiative transfer to biophysical processes in
886 vegetated canopies, Phd, faculty of geo-information science and earth observation, University of Twente,
887 Enschede, The Netherlands, 1-157 pp., 2011.

888 Vinukollu, R. K., Meynadier, R., Sheffield, J., and Wood, E. F.: Multi-model, multi-sensor estimates of
889 global evapotranspiration: climatology, uncertainties and trends, *Hydrol Process*, 25, 3993-4010,
890 10.1002/hyp.8393, 2011a.

891 Vinukollu, R. K., Wood, E. F., Ferguson, C. R., and Fisher, J. B.: Global estimates of evapotranspiration for
892 climate studies using multi-sensor remote sensing data: Evaluation of three process-based approaches,
893 *Remote Sensing of Environment*, 115, 801-823, 10.1016/j.rse.2010.11.006, 2011b.

894 Wan, Z., and Li, Z. L.: Radiance - based validation of the V5 MODIS land - surface temperature product,
895 *International Journal of Remote Sensing*, 29, 5373-5395, 10.1080/01431160802036565, 2008.

896 Collection-5 MODIS land surface temperature products users' guide.
897 <http://www.icess.ucsb.edu/modis/LstUsrGuide/usrguide.html>, 2009.

898 Wang, A., and Zeng, X.: Evaluation of multireanalysis products with in situ observations over the Tibetan
899 Plateau, *J. Geophys. Res.*, 117, D05102, 10.1029/2011jd016553, 2012.

900 Wang, A., Barlage, M., Zeng, X., and Draper, C. S.: Comparison of land skin temperature from a land
901 model, remote sensing, and in-situ measurement, *Journal of Geophysical Research: Atmospheres*,
902 2013JD021026, 10.1002/2013jd021026, 2014.

903 Wang, G., Huang, J., Guo, W., Zuo, J., Wang, J., Bi, J., Huang, Z., and Shi, J.: Observation analysis of land-
904 atmosphere interactions over the Loess Plateau of northwest China, *J. Geophys. Res.*, 115, D00K17,
905 10.1029/2009jd013372, 2010.

906 Wang, K., Wang, P., Li, Z., Cribb, M., and Sparrow, M.: A simple method to estimate actual
 907 evapotranspiration from a combination of net radiation, vegetation index, and temperature, *Journal of*
 908 *Geophysical Research: Atmospheres*, 112, D15107, 10.1029/2006jd008351, 2007.

909 Wang, K., and Liang, S.: An improved method for estimating global evapotranspiration based on satellite
 910 determination of surface net radiation, vegetation index, temperature, and soil moisture, *Journal of*
 911 *Hydrometeorology*, 9, 712-727, 10.1175/2007jhm911.1, 2008.

912 Wang, S., Zhang, Y., Lv, S., Liu, H., and Shang, L.: Estimation of turbulent fluxes using the flux-variance
 913 method over alpine meadows surface in eastern Tibetan Plateau, *Advances in Atmospheric Sciences*, 30,
 914 411-424, 10.1007/s00376-012-2056-1, 2013.

915 Wu, G., Liu, Y., He, B., Bao, Q., Duan, A., and Jin, F.-F.: Thermal controls on the Asian summer monsoon,
 916 *Sci. Rep.*, 2, 404, 10.1038/srep00404 (2012), 2012.

917 Yan, H., Wang, S. Q., Billesbach, D., Oechel, W., Zhang, J. H., Meyers, T., Martin, T. A., Matamala, R.,
 918 Baldocchi, D., Bohrer, G., Dragoni, D., and Scott, R.: Global estimation of evapotranspiration using a leaf
 919 area index-based surface energy and water balance model, *Remote Sensing of Environment*, 124, 581-
 920 595, 2012.

921 Yang, K., Koike, T., Fujii, H., Tamagawa, K., and Hirose, N.: Improvement of surface flux parametrizations
 922 with a turbulence-related length, *Quarterly Journal of the Royal Meteorological Society*, 128, 2073-2087,
 923 2002.

924 Yang, K., Ding, B., Qin, J., Tang, W., Lu, N., and Lin, C.: Can aerosol loading explain the solar dimming over
 925 the Tibetan Plateau?, *Geophys. Res. Lett.*, 39, L20710, 10.1029/2012gl053733, 2012.

926 Yao, T., Wang, Y., Liu, S., Pu, J., Shen, Y., and Lu, A.: Recent glacial retreat in High Asia in China and its
 927 impact on water resource in Northwest China, *Science in China Series D: Earth Sciences*, 47, 1065-1075,
 928 10.1360/03yd0256, 2004.

929 Yao, Y., Liang, S., Cheng, J., Liu, S., Fisher, J. B., Zhang, X., Jia, K., Zhao, X., Qin, Q., Zhao, B., Han, S., Zhou,
 930 G., Zhou, G., Li, Y., and Zhao, S.: MODIS-driven estimation of terrestrial latent heat flux in China based on
 931 a modified Priestley–Taylor algorithm, *Agricultural and Forest Meteorology*, 171–172, 187-202,
 932 <http://dx.doi.org/10.1016/j.agrformet.2012.11.016>, 2013.

933 Yu, G.-R., Wen, X.-F., Sun, X.-M., Tanner, B. D., Lee, X., and Chen, J.-Y.: Overview of ChinaFLUX and
 934 evaluation of its eddy covariance measurement, *Agricultural and Forest Meteorology*, 137, 125-137,
 935 <http://dx.doi.org/10.1016/j.agrformet.2006.02.011>, 2006.

936 Yuan, W., Liu, S., Yu, G., Bonnefond, J.-M., Chen, J., Davis, K., Desai, A. R., Goldstein, A. H., Gianelle, D.,
 937 Rossi, F., Suyker, A. E., and Verma, S. B.: Global estimates of evapotranspiration and gross primary
 938 production based on MODIS and global meteorology data, *Remote Sensing of Environment*, 114, 1416-
 939 1431, <http://dx.doi.org/10.1016/j.rse.2010.01.022>, 2010.

940 Zhang, C., Chen, F., Miao, S., Li, Q., Xia, X., and Xuan, C.: Impacts of urban expansion and future green
 941 planting on summer precipitation in the Beijing metropolitan area, *Journal of Geophysical Research:*
 942 *Atmospheres*, 114, D02116, 10.1029/2008jd010328, 2009a.

943 Zhang, K., Kimball, J. S., Nemani, R. R., and Running, S. W.: A continuous satellite-derived global record
 944 of land surface evapotranspiration from 1983 to 2006, *Water Resources Research*, 46, W09522,
 945 10.1029/2009wr008800, 2010.

946 Zhang, L., Li, Y., Li, Y., and Zhao, X.: Seasonal changes of turbulent fluxes at a typical agricultural site in
 947 the Chengdu Plain based on quality-controlled data, *Journal of the Meteorological Society of Japan. Ser.*
 948 *II*, 90C, 195-202, 2012.

949 Zhang, X., Ren, Y., Yin, Z.-Y., Lin, Z., and Zheng, D.: Spatial and temporal variation patterns of reference
 950 evapotranspiration across the Qinghai-Tibetan Plateau during 1971&-2004, *J. Geophys. Res.*, 114,
 951 D15105, 10.1029/2009jd011753, 2009b.

952 Zhao, B., Yan, Y., Guo, H., He, M., Gu, Y., and Li, B.: Monitoring rapid vegetation succession in estuarine
953 wetland using time series MODIS-based indicators: An application in the Yangtze River Delta area,
954 Ecological Indicators, 9, 346-356, <http://dx.doi.org/10.1016/j.ecolind.2008.05.009>, 2009.
955 Zhong, L., Su, Z., Ma, Y., Salama, M. S., and Sobrino, J. A.: Accelerated changes of environmental
956 conditions on the Tibetan Plateau caused by climate change, Journal of Climate, 24, 6540-6550,
957 10.1175/jcli-d-10-05000.1, 2011.
958 Zhou, L., and Huang, R.: Interdecadal variability of sensible heat flux in arid and semi-arid region of
959 Northwest China and its relationship to summer precipitation in China (in Chinese), Chinese J. Atmos.
960 Sci., 32, 1276-1288, 2008.
961 Zhou, L., and Huang, R.: An assessment of the quality of surface sensible heat flux derived from
962 reanalysis data through comparison with station observations in Northwest China, Advances in
963 Atmospheric Sciences, 27, 500-512, 10.1007/s00376-009-9081-8, 2010.
964 Zhu, X., Liu, Y., and Wu, G.: An assessment of summer sensible heat flux on the Tibetan Plateau from
965 eight data sets, Science China Earth Sciences, 55, 779-786, 10.1007/s11430-012-4379-2, 2012.

966

967

968

969

970

971

972

973

974

975

976

977

978

979 Table 1. Input datasets used for calculating land surface fluxes for China (see Sections 2 and 3
980 for an explanation of abbreviations)

Variables	Data source	Temporal resolution	Availability	Domain	Spatial resolution (degrees)	Method
SWD	ITPCAS	3 hours	1979-2010	China land	0.1	Reanalysis
SWU	ITPCAS& GlobAlbedo	3 hours	1982-2009	China land	0.1	Satellite&Reanalysis
LWD	ITPCAS	3 hours	1979-2010	China land	0.1	Reanalysis
LWU	MOD11C3& MYD11C3 V5&Emis of Chen et al. 2013	1 month	2000-2012	China land	0.05	Satellite
Ta	ITPCAS	3 hours	1979-2010	China land	0.1	Reanalysis
Q	ITPCAS	3 hours	1979-2010	China land	0.1	Reanalysis
Ws	ITPCAS	3 hours	1979-2010	China land	0.1	Reanalysis
P	ITPCAS	3 hours	1979-2010	China land	0.1	Reanalysis
LST	MOD11C3 V5& MYD11C3 V5	1 month	2000-2012	Global	0.05	Satellite
h _c	GLAS&SPOT VEGETATION	1 month	2000-2012	China land	0.01	Satellite
A	GlobAlbedo	1 month	2000-2010	Global	0.05	Satellite
NDVI	SPOT VEGETATION	10 days	1998-2012	Global	0.01	Satellite
LAI	MOD15A2& MCD15A2	8 days	Feb, 2000-Jul, 2002 Aug, 2002-2012/	Global	0.01	Satellite

981

982

983

Table 2. Flux tower sites supplying measurement data for product validation

	Lat[deg]/ Lon[deg]	Land cover	Eddy covariance	Radiometer	Measurement period	Site elevation (m)	Reference
WJ	30.4200N/ 103.5000E	Crop	CSAT3,Licor7500 (10 HZ)	CNR-1	Mar 2008 - Aug 2009	539	Zhang et al. (2012)
MQ	33.8872N/ 102.1406E	Alpine meadow	CSAT3,Licor7500 (10 HZ)	CNR-1	Apr 2009 - May 2010	3439	Wang et al. (2013)
AL	33.3905N/ 79.7035E	Bare soil	CSAT3,Licor7500 (10 HZ)	CNR-1	Jul 2010 - Dec 2010	4700	Ma et al. (2008b)
BJ	31.3686N/ 91.8986E	Alpine grass	CSAT3,Licor7500 (10 HZ)	CNR-1	Jan 2008 - Dec 2010	4520	Ma et al. (2011)
MY	40.6038N/ 117.3233E	Orchard	CSAT3,Licor7500 (10 HZ)	CNR-1	Jan 2008 - Dec 2010	350	Liu et al. (2013b)
DX	39.6213N/ 116.4270E	Crop	CSAT3,Licor7500 (10 HZ)	CNR-1	Jan 2008 - Dec 2010	100	Liu et al. (2013b)
GT	36.5150N/ 115.1274E	Crop	CSAT3,Licor7500 (10 HZ)	CNR-1	Jan 2008 - Dec 2010	30	Liu et al. (2013b)
YC	36.9500N/ 116.600E	Crop	CSAT3,Licor7500 (10 HZ)	CNR-1	Oct 2002 - Oct 2004	13	Flerchinger et al. (2009)
DT	31.5169N/ 121.9717E	Wetland	CSAT3,Licor7500 (10 HZ)	CNR-1	Jan 2005 - Dec 2007	5	Zhao et al. (2009)
SC	35.95N/ 104.133E	Dry land	CSAT3,Licor7500 (10 HZ)	CNR-1	Jan 2007 - Dec 2008	1965	Huang et al. (2008)
WS	36.6488N/ 116.0543E	Winter wheat / summer maize	CSAT3,Licor7500 (10 HZ)	CNR-1	Jan 2006 - Dec 2008	30	Lei and Yang (2010a)

994

995

996

997

998 Table 3. Comparison of accuracy of our flux data product and GLDAS against in-situ
999 measurements from 11 Chinese flux towers. MB is mean of observation minus model simulation.

1000

		Energy flux					Radiation flux				
		H (Wm ⁻²)	LE (Wm ⁻²)	G0 (Wm ⁻²)	Rn (Wm ⁻²)	Mean	SWD (Wm ⁻²)	SWU (Wm ⁻²)	LWD (Wm ⁻²)	LWU (Wm ⁻²)	Mean
Our flux data product	Slope	0.39	0.9	0.87	0.92	0.77	0.95	0.68	0.91	0.95	0.87
	Intercept	-0.5	-6.1	6.1	-20.2	-8.2	13.6	10.9	-0.66	16.6	9.9
	RMSE	21.5	21.9	11.7	36.2	22.8	28.3	10.2	32.8	9.6	20.2
	MB	14.7	10.1	-5.7	26.3	11.4	-5.7	-0.65	28.9	2.4	6.2
	R	0.41	0.85	0.50	0.86	0.66	0.89	0.78	0.98	0.99	0.91
	Sample	280	284	197	313	270	310	307	307	307	308
GLDAS	Slope	0.77	0.87	0.58	1.0	0.81	0.99	0.75	0.87	1.0	0.90
	Intercept	20.83	5.1	-1.34	8.0	8.2	34.9	13.1	27.7	-4.5	17.8
	RMSE	26.6	20.6	6.7	17.9	17.9	45.6	15.9	19.2	11.1	23.0
	MB	-15.8	0.75	3.0	-10.4	-5.6	-32.87	-4.6	13.5	-3.2	-6.8
	R	0.46	0.80	0.61	0.95	0.71	0.87	0.65	0.99	0.98	0.87
	Sample	249	250	162	281	236	275	272	272	275	274

1001

1002

1003

1004

1005

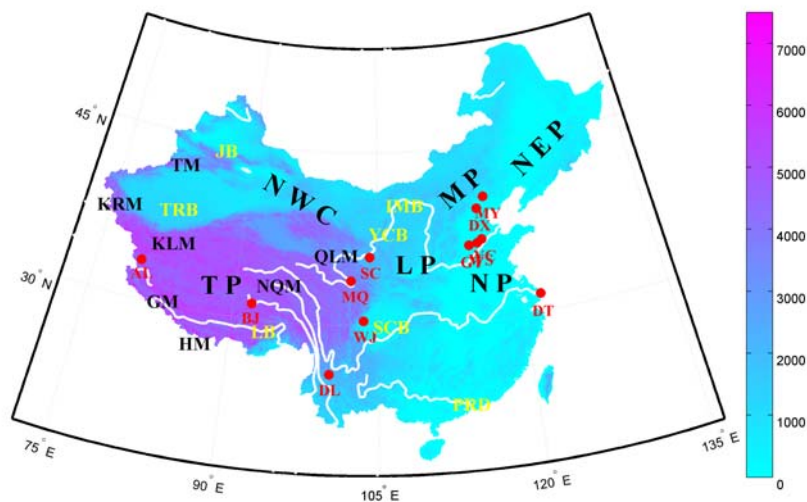
1006

1007

1008

1009

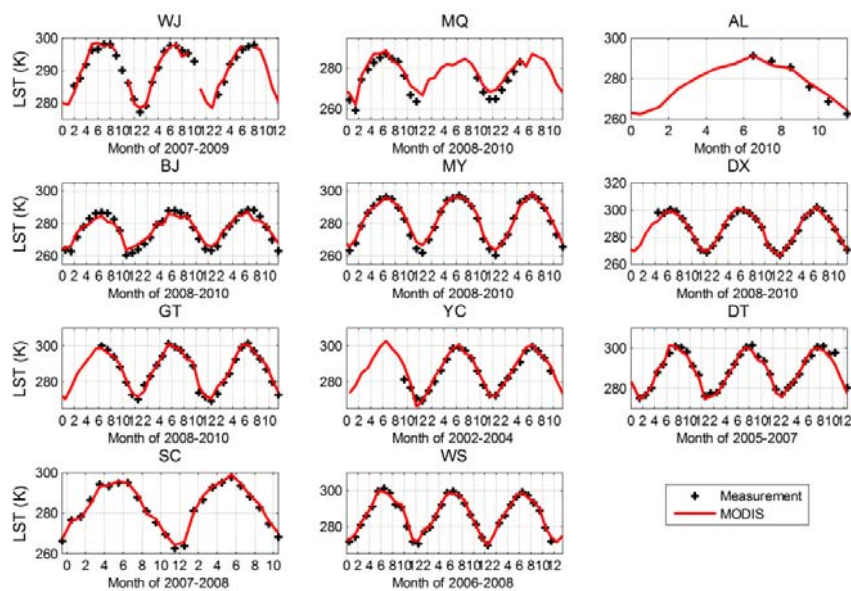
1010



1021
1022

1023 | Figure 1. A DEM/NDVI map of the Chinese landmass ~~based on SPOT satellite data~~. The symbols
1024 indicate major physical phenomena: Tibetan Plateau (TP), northwestern China (NWC), inner
1025 Mongolian Plateau (MP), Loess Plateau (LP), North China Plain (NP), northeastern China Plain
1026 (NEP); Pearl River delta (PRD), Sichuan (SCB), Yinchuan (YCB), the inner Mongolian (IMB),
1027 and Lasha (LB), Tarim (TRB), Junggar (JB) basins; the Himalaya (HM), Ganges (GM), Kunlun
1028 (KL), Karakorum (KRM), Tianshan (TM), Nyainqentanglha (NQM) and Qilian mountain (QLM)
1029 ranges. The plateau and plain letter symbols are in red type. The basins letter symbols are in
1030 green type. The flux station letter symbols are in yellow type. Blue/White lines show several of
1031 the major rivers in China. ~~Black lines indicate the borders of provinces.~~

1032
1033
1034
1035
1036
1037



Formatted: Font: Times New Roman, 12 pt

Fig. 2 Time series comparison of monthly averaged LST derived from MOD11C3&MYD11C3 and in-situ measurements.

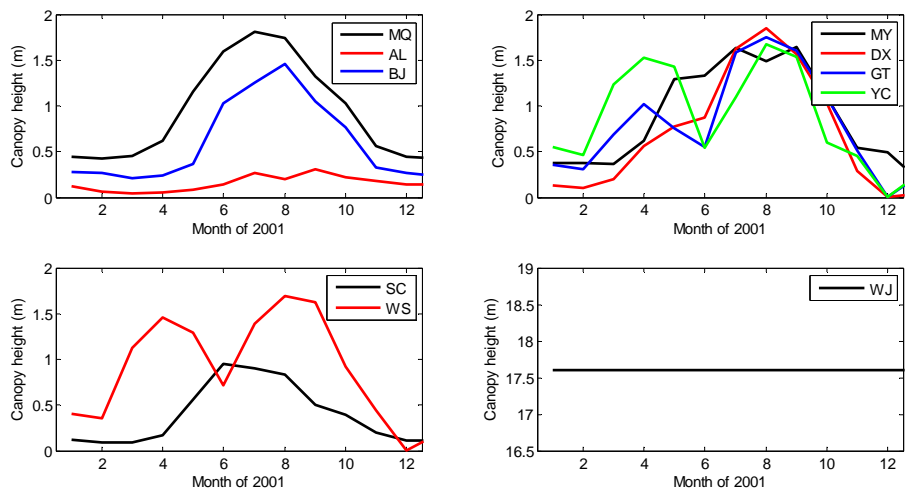
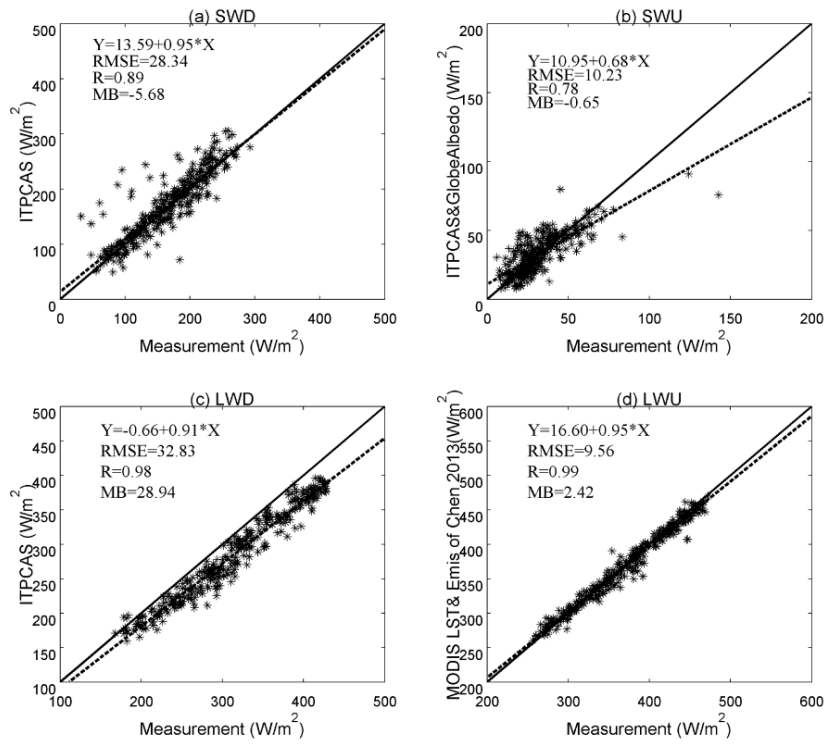


Fig. 3 Monthly variation of canopy height at the 10 flux stations

Formatted: Font: Times New Roman, 12 pt

Formatted: Centered

Formatted: Space After: 0 pt, Line spacing: Double



Formatted: Font: Times New Roman, 12 pt

Figure 4 Scatter point for downward shortwave (SWD), upward shortwave (SWU), downward longwave (LWD), and upward longwave (LWU) radiation against in-situ measurement.

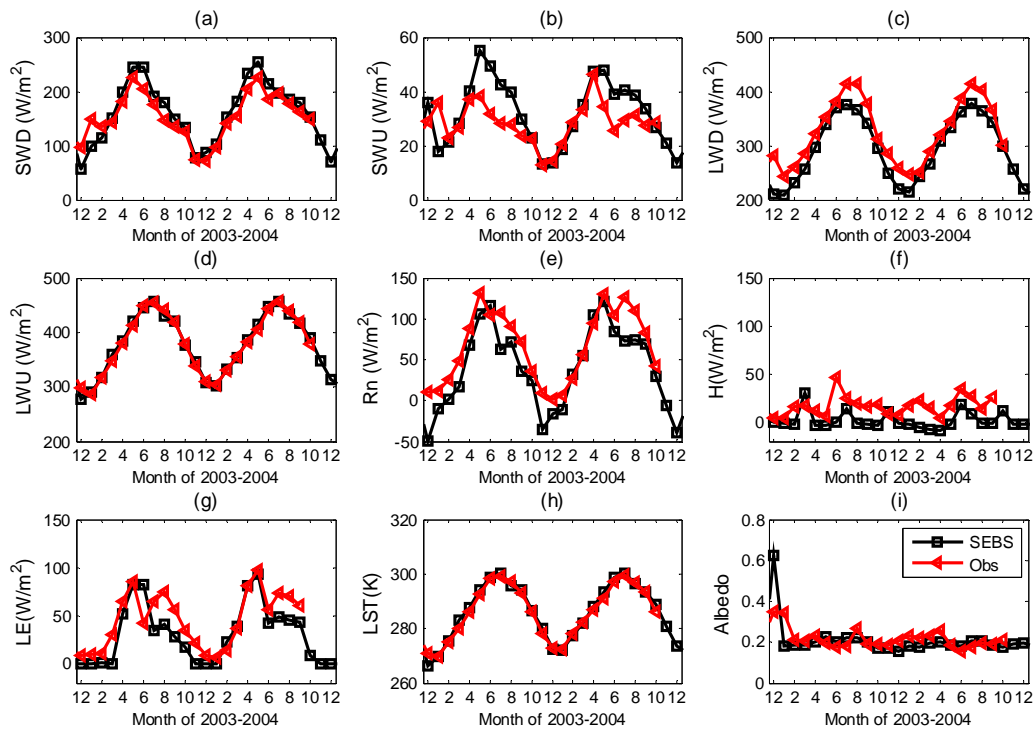
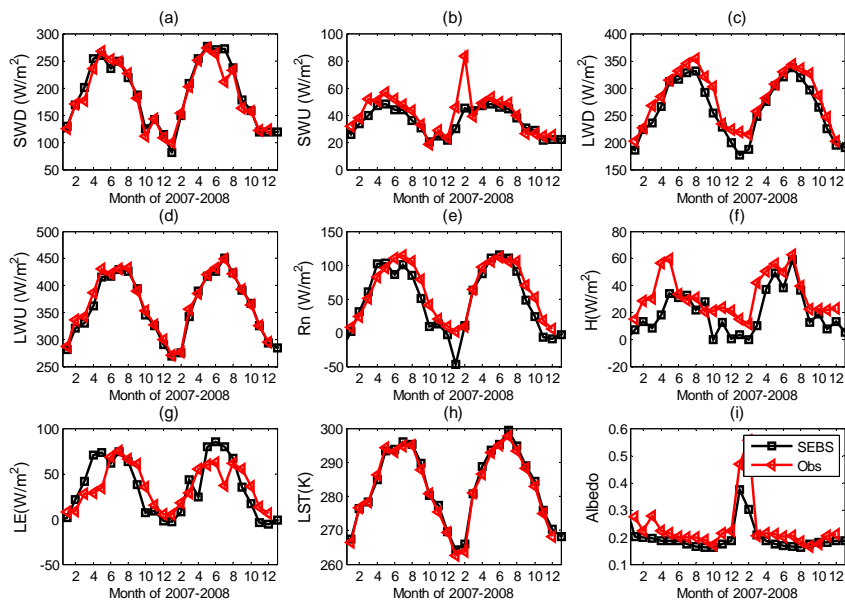


Figure 52. Time-series comparison of SEBS input and output variables against measurements at Yucheng station. Black lines are SEBS results; red lines are measured values.



1063

1064 | Figure 63. Time-series comparison of SEBS input and output variables against measurements at
 1065 SC station. Black lines are SEBS results; red lines are measured values.

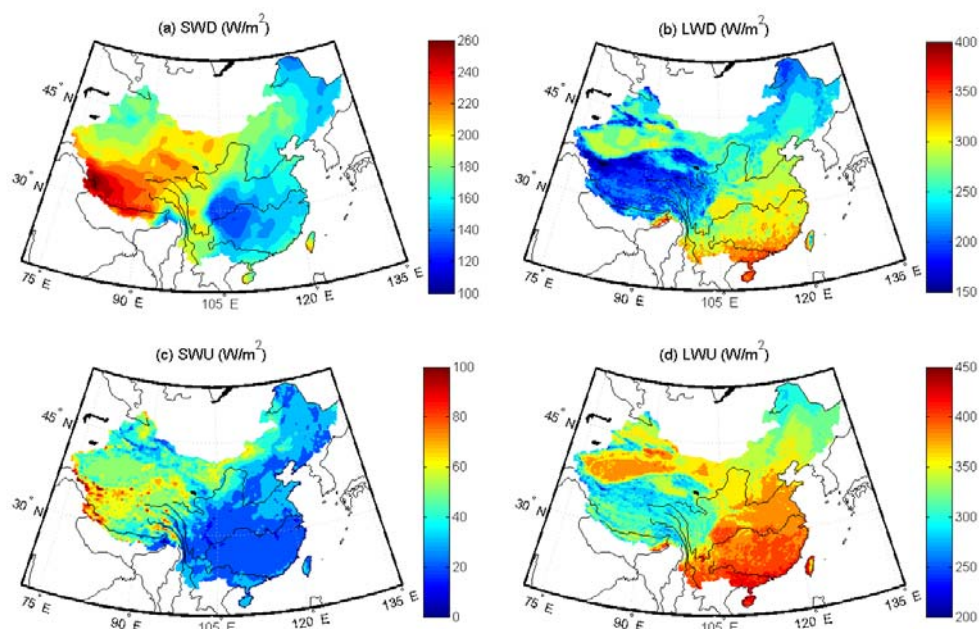
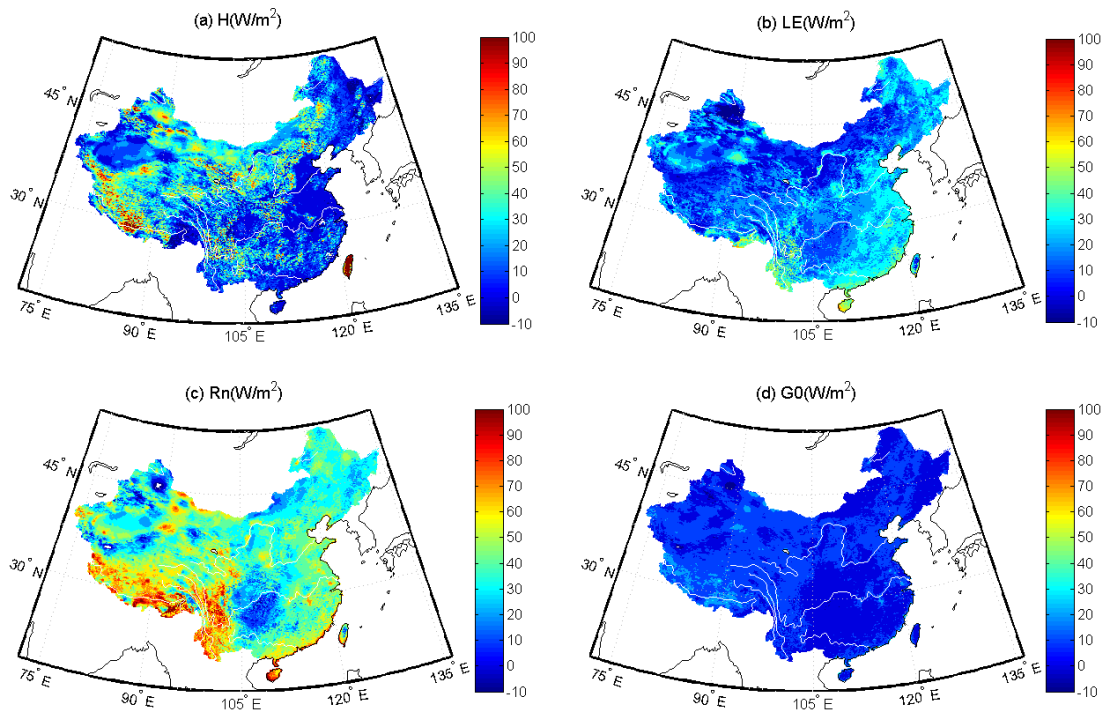


Figure 74. Maps of annual average (a) downward short-wave radiation (SWD), (b) downward long-wave radiation (LWD), (c) upward short-wave radiation (SWU), and (d) upward long-wave radiation (LWU) from 2001 to 2010. Black lines show several major rivers in China.



1074

1075 | Figure 85. Maps of multiyear (2001–2010) means of retrieved fluxes: (a) sensible heat flux (H),
 1076 (b) latent heat flux (LE), (c) net radiation (Rn), and (d) ground heat flux (G0). White lines show
 1077 several major rivers in China.

1078

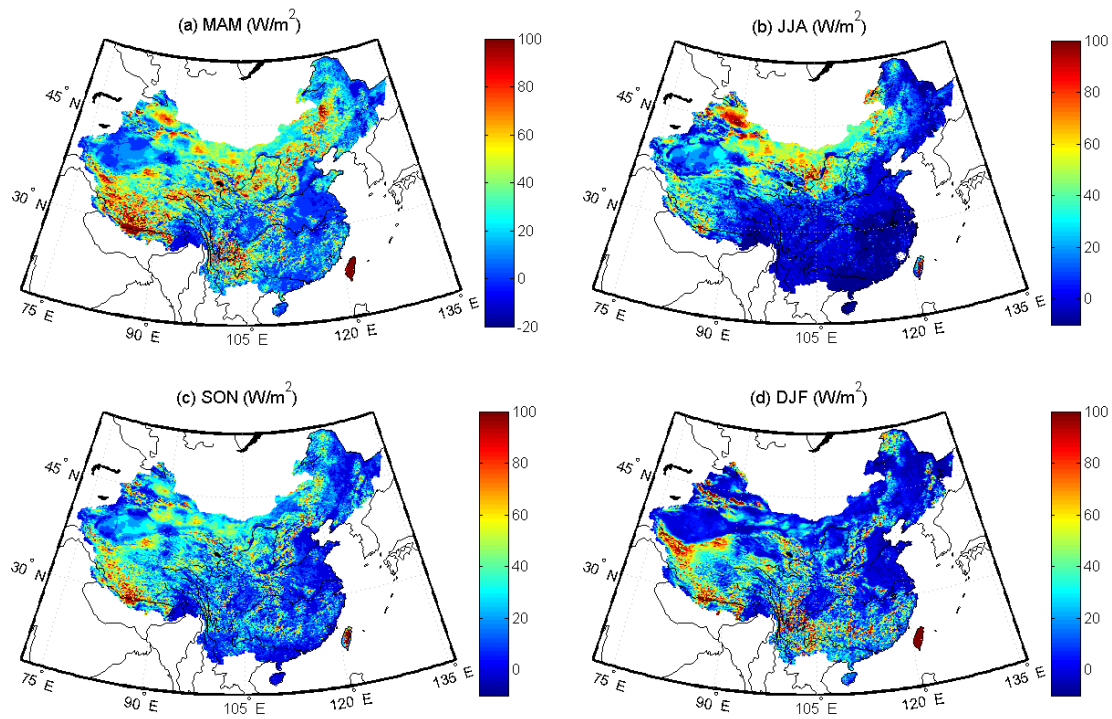
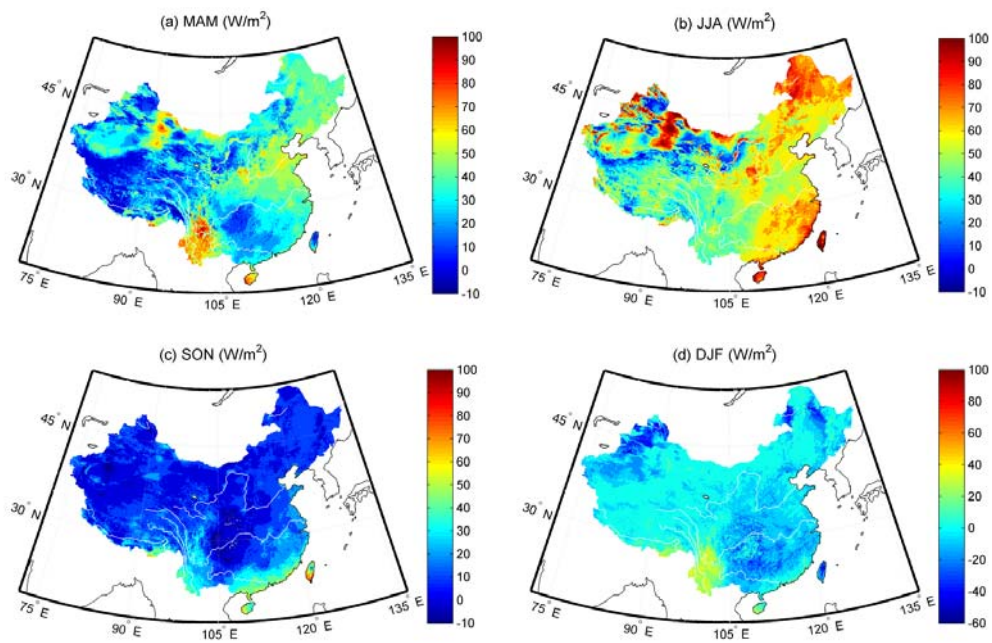


Figure 96. Maps of seasonal average sensible heat flux for (a) March-May (MAM), (b) June-August (JJA), (c) September-November (SON), and (d) December- February (DJF) from 2001 to 2010. Black lines show several major rivers in China.



1085
1086
1087 | Figure 107. Maps of seasonal average latent heat flux for (a) March-May (MAM), (b) June-
1088 August (JJA), (c) September-November (SON), and (d) December- February (DJF) from 2001 to
1089 2010. White lines show several major rivers in China.

1096

1097

1098

1099

1100

1101

1102

1103

1104

1105

1106

1107

1108

1109

1110

1111

1112

1113

1114

1115

1116

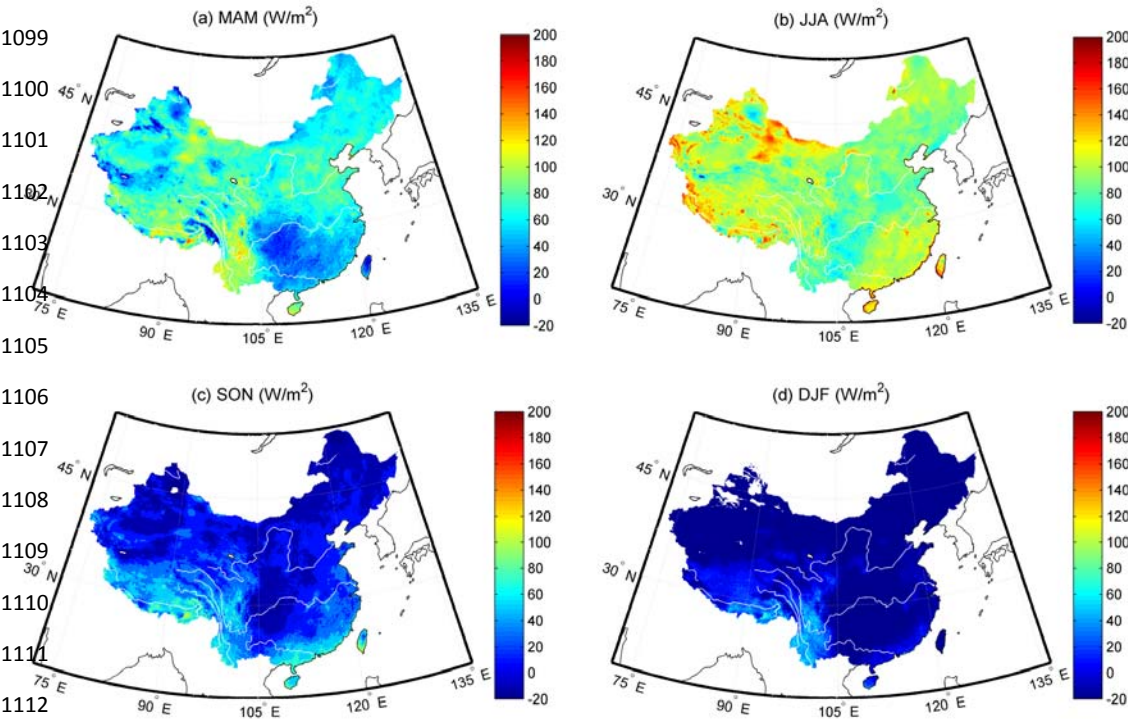
1117

1118

1119

1120

1121



1115 | Figure 118. Maps of seasonal average net radiation for (a) March-May (MAM), (b) June-August
1116 (JJA), (c) September-November (SON), and (d) December- February (DJF) from 2001 to 2010.
1117 White lines show several major rivers in China.

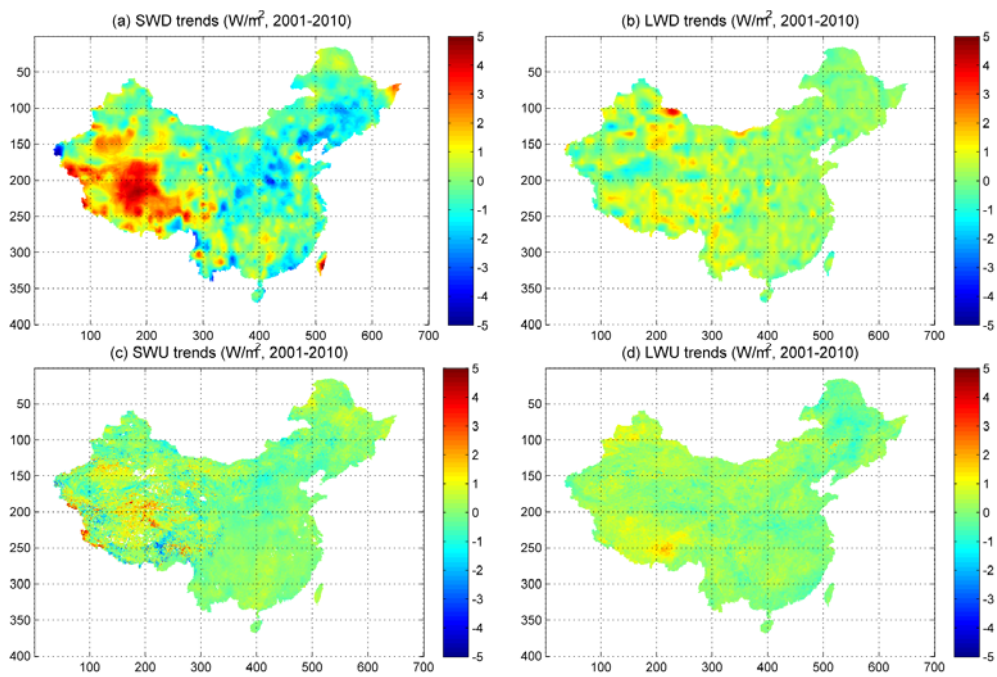


Figure 129. Spatial trends of (a) SWD (downward short-wave), (b) LWD (downward long-wave), (c) SWU (upward short-wave), and (d) LWU (upward long-wave radiation) for the Chinese landmass from 2001 to 2010.

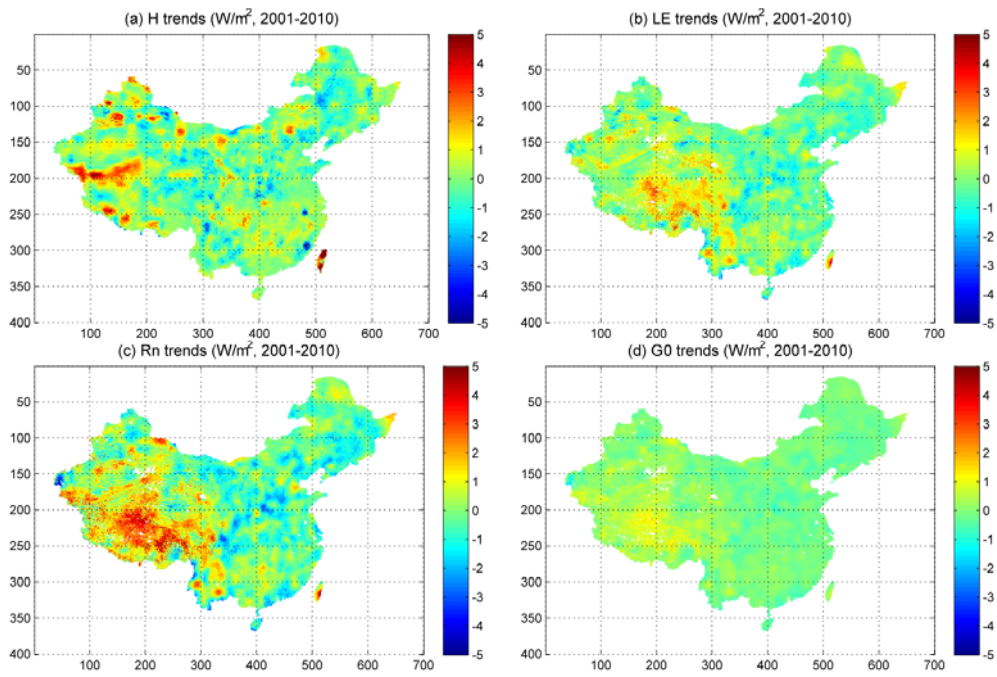


Figure 130. Spatial trends of (a) sensible heat flux (H), (b) latent heat flux (LE), (c) net radiation (Rn), and (d) ground heat flux (G0) on the Chinese landmass from 2001 to 2010.

List Paragraph, Outline numbered + Level: 2 + Numbering Style: 1, 2, 3, ... + Start at: 1 +

Alignment: Left + Aligned at: 0 cm + Indent at: 0.85 cm